



# Computational Enhancement of a Mixed 3D Beam Finite Element with Warping and Damage

Paolo Di Re<sup>ID</sup>, Daniela Addressi<sup>ID</sup>

Department of Structural and Geotechnical Engineering, Sapienza University of Rome, Via Eudossiana 18, Rome, 00184, Italy  
Email: paolo.dire@uniroma1.it, daniela.addressi@uniroma1.it

Received July 12 2021; Revised September 17 2021; Accepted for publication October 16 2021.

Corresponding author: D. Addressi (daniela.addressi@uniroma1.it)

© 2022 Published by Shahid Chamran University of Ahvaz

**Abstract.** This paper describes the computational aspects of the beam Finite Element formulation recently developed by the authors to simulate the nonlinear response of structural members subjected to shear and torsion, accounting for cross-section warping. The paper focuses on an efficient consistent solution algorithm that by-passes the iterative procedure required in force-based and mixed Finite Elements and makes the model easy to be implemented in a standard code. Moreover, it proposes a new non-iterative technique to condense out the stress components derived by the three-dimensional constitutive response and not directly included in the fiber section formulation. The efficiency and accuracy of the proposed numerical model are validated by simulating the response of steel and reinforced concrete structural members.

**Keywords:** Mixed Finite Element, Enhanced beam formulation, Warping, Nonlinear analysis, Damage.

## 1. Introduction

The adoption of beam Finite Elements (FE) is the most common and convenient approach for the analysis of large-scale framed structures (Fig. 1), as these result computationally more efficient than the more sophisticated plate/shell and three-dimensional (3D) models [1, 2]. Indeed, although these latter usually offer higher accuracy and permit a more detailed description of plasticity, fracture, damage and bond phenomena, typically occurring in frame structures, they are often too computationally demanding so that their use is limited to the analysis of single members or very small structures.

Among the different beam models, force-based and mixed formulations have proven superior performances than the classical displacement-based models under large inelastic and cyclic deformations, although the slight increase of the computational cost for the more involved element state determination. Indeed, with respect to the displacement-based approaches, force-based and two- or three-field mixed models with independent interpolation of displacements, strains and/or stresses [3-5], require coarser meshes to accurately reproduce the structural behavior in the nonlinear range of material response, thus involving a significant computational saving [6].

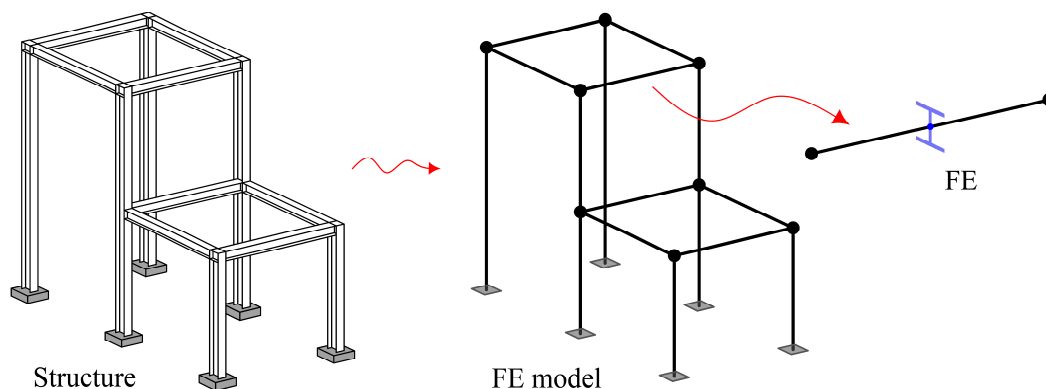


Fig. 1. Example of FE modeling of a framed structures



However, all the mentioned formulations usually assume the element cross-section as rigid and, thus, neglect the effects of warping. In many relevant cases, such as bridges, shear walls or thin-walled frames, these effects result essential to correctly describe the structural behavior. For damaging materials, such as concrete or innovative fiber reinforced composites, the influence of shear and torsional loads increases, making the analysis of these structures a challenging problem.

Many authors proposed enhanced formulations which extend the Timoshenko beam model and account for the warping deformations of the cross-section, basing on different approaches. Among them, some recent proposals are worth to be mentioned and extensive reviews are given by other authors [7, 8]. Bairàn [9] proposed a generalized beam model that describes non-uniform shear strain/stress distributions over the beam cross-section. As assumed in this work, the model by Bairàn considers cross-section displacements as the composition of two contributions: one related to plane-section displacements and the other related to out-of-plane warping. However, as opposed to the proposed model, transverse deformations of the cross-section are also included by ensuring the equilibrium conditions between the fibers composing the element. Thus, compatibility between concrete and transverse reinforcement is also included. Many refinements of this first proposal were later presented by Bairàn himself and co-authors, among which the models in [10, 11] deserve particular attention. The model in [10] is a simplified version of that in [9], where beam description is limited to 2D analysis and shear and vertical strain distributions are assumed to be composed by a series of polynomial shape functions. Model in [11] exploits a complementary displacement field, defined as a weighted sum of b-splines functions over the cross-section domain, to improve computational performances. An approach similar to that in [9] has been also adopted in the recent work by Kagermanov and Ceresa [12]. Saritas [13] proposed a 2-node force-based Timoshenko FE that assumes an assigned distribution for the shear strains over the cross-section due to shear forces. This distribution is computed under linear elastic material assumption and used to account for cross-section shear warping also under nonlinear material behavior. Ferradi et al. [14], Vieira et al. [15] and Dikaros et al. [16] described the cross-section out-of-plane displacements through the composition of independent warping modes, which are evaluated by imposing equilibrium conditions at the linear stage and are used as interpolation shape functions during the entire loading process. Capdevielle et al. [17] followed a similar approach, thus updating the warping functions at each time step to improve the model accuracy under nonlinear responses. Finally, Genoese et al. [18] defined a mixed Hellinger-Reissner beam model based on an accurate description of the stress fields, evaluated as the sum of the exact De Saint Venant contribution and some further terms due to variable warping.

This paper presents computational enhancements of the 2-node 3D four-field mixed beam FE, originally proposed by Le Corvec [19] for the analysis of thin-walled steel members, and later extended by Di Re et al. to reinforced concrete (RC) structures [20-22] and dynamic loading conditions [23]. The model accounts for the out-of-plane cross-section warping by introducing a specific displacement field in addition to those due to the classical displacements relying on the plane-section assumption. The cross-section warping is interpolated through a variable number of local degrees of freedom (DOF) added to those commonly used for the beam FE. The local distributions of strains and stresses are described introducing a fiber cross-section discretization that accounts for the coupling of axial, flexural, shear and torsional effects in terms of material response. A similar approach based on shape functions was proposed by Gruttmann et al. [24] and Lee et al. [25] and has been recently adopted by Yoon et al. [26] and Khoder et al. [27]. The latter apply the method to describe in-plane stretching of the cross-section and explicitly model transverse reinforcements. However, they adopt a 2D FE discretization of the element cross-sections and consider displacement-based beam FE formulation.

After recalling the main issues of the 3D beam FE formulation, the paper focuses on the computational details required for the implementation of the model in general FE codes and provides efficient algorithms to solve the element state determination in a step-by-step analysis scheme. In the original proposal of the model, Le Corvec [19] defined an iterative solution algorithm to enforce simultaneously equilibrium and compatibility conditions at each step of the global solution scheme. By slightly extending the classical iterative algorithm adopted for standard force-based beam FEs [3, 28], this performs a simple updating of the section deformations with the inclusion of warping related terms. Although the algorithm proved to be efficiently applicable for the analysis of elastic and elasto-plastic beams, it is not suitable for the analysis of degrading elements, as it fails to converge when cross-section strength tends to vanish due to softening of the material. Following the idea proposed by Neuenhofer et al. [29] for standard force-based beam FEs, an enhanced procedure, with respect to that proposed by Le Corvec, is presented here. This is based on the evaluation of warping displacement and force increments at each iteration, which are used to correctly compute internal residual quantities, so that internal residual energy convergence is ensured. Moreover, by simply setting the maximum number of iterations to one, this works as a non-iterative scheme, i.e. permits to by-pass the iterations required at the element level, and significantly improves computational efficiency [30].

An elasto-plastic constitutive law based on the classical J2 plasticity [31] is adopted to simulate the steel frame structural response, while the 3D plastic-damage constitutive relationship proposed by Di Re et al. [21] is used to simulate the response of concrete and investigate the effects of section warping on the degrading behavior of RC frames. The model formulation is reviewed, and an efficient predictor-corrector solution procedure is proposed to perform the material state determination. Finally, to condense out the stress components derived by the 3D constitutive response and not directly included in the fiber section formulation, an iterative technique is often adopted [32-34], which results much time consuming in nonlinear analysis. In this paper, an effective non-iterative nonlinear procedure is proposed, that takes advantage of the solution scheme at the element and global levels and avoids the inner loop.

The model is implemented in a FE code and its accuracy and numerical efficiency is shown by performing numerical simulations of RC and steel structures under coupled multi-axial strain and stress states. Two types of RC specimens are considered: a U-shaped shear wall under cyclic horizontal loading and a series of prismatic beams under monotonic torsional loads. For both applications, discussion focuses on the interaction of cross-section warping and damaging process evolution. Moreover, the response of a steel frame is reproduced to investigate the performance of the proposed model in capturing the warping transmission at the beam-column connection joint.

## 2. Description of the 3D Beam FE

### 2.1 Element kinematics

The 3D beam element kinematics is described in the local basic reference system  $(x, y, z)$  that removes the rigid body motions, according to the equilibrated approach [5, 28, 35]. The  $x$ -axis is parallel to the direction going from element node  $i$  to node  $j$ , while  $y$  and  $z$  are the cross-section principal axes (Fig. 2a).

$L$  is the undeformed element length, corresponding to the distance between the two end nodes. Vector  $\mathbf{v}$  collects the element basic displacements, resulting as:



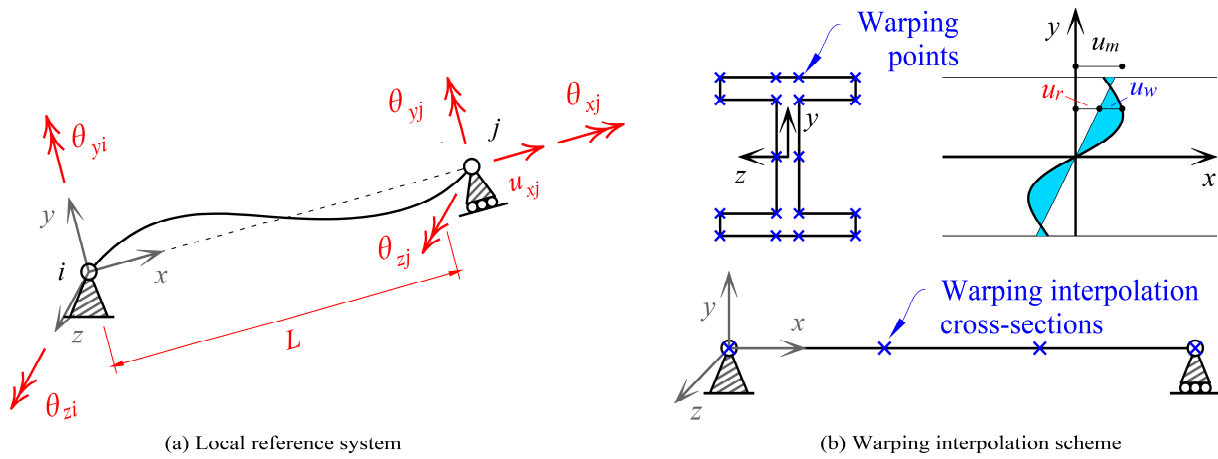


Fig. 2. Basic element displacement in the local reference system and example of warping displacement interpolation scheme.

$$\mathbf{v} = \{u_{xj} \ \theta_{zi} \ \theta_{zj} \ \theta_{xj} \ \theta_{yi} \ \theta_{yj}\}^T \tag{1}$$

where  $u_{xj}$  is the translation of node  $j$  parallel to  $x$ ,  $\theta_{zi/j}$  and  $\theta_{yi/j}$  are the rotations at node  $i/j$  about the  $z$ - and  $y$ -axis, respectively, and  $\theta_{xj}$  is the rotation at node  $j$  about the  $x$ -axis. These are derived from the twelve nodal DOFs, i.e., the three translations and three rotations at each node listed in the displacement vector  $\mathbf{u}$ , according to the following expression:

$$\mathbf{v} = \mathbf{a}_g \mathbf{u} \tag{2}$$

where  $\mathbf{a}_g$  is the compatibility matrix [28].

The displacement fields at the cross-section material point  $m$ , namely  $u_m(x,y,z)$ ,  $v_m(x,y,z)$  and  $w_m(x,y,z)$  along the axes  $x$ ,  $y$  and  $z$ , respectively, are collected in the vector  $\mathbf{u}_m(x,y,z)$ , defined as:

$$\mathbf{u}_m(x,y,z) = \mathbf{u}_s(x,y,z) + \mathbf{u}_w(x,y,z) = \mathbf{a}_s(y,z)\mathbf{u}_s(x) + \mathbf{u}_w(x,y,z) \tag{3}$$

Term  $\mathbf{u}_s(x,y,z)$  in Eq. (3) is the contribution of the plane-section motions, which are collected in  $\mathbf{u}_s(x)$ , being  $\mathbf{a}_s(y,z)$  the section compatibility matrix. The contribution of the cross-section warping is, then, added, as in [9]. Assuming the cross-section as rigid in its plane,  $\mathbf{u}_w(x,y,z)$  contains only the out-of-plane displacement field, i.e.,  $\mathbf{u}_w(x,y,z) = \{u_w(x,y,z) \ 0 \ 0\}^T$ .

The warping displacement field  $u_w(x,y,z)$  is interpolated according to the classical approach based on the use of shape functions, independently considering the variation along the element  $x$ -axis and that over the cross-section [19-20].  $n_w$  interpolation points are located along the  $x$ -axis, corresponding to controlling cross-sections.  $m_w$  warping DOFs are, then, introduced on each cross-section to represent  $u_w(x,y,z)$  (Fig. 2b), using either two-dimensional (2D) Lagrange or Hermite interpolation polynomials  $M_j(x)$ . Thus, the warping displacement field at the  $i$ -th interpolation point results as:

$$u_{w,i}(x_i,y,z) = \sum_{j=1}^{m_w} M_j(y,z)u_{w,ij} = \mathbf{M}(y,z)\mathbf{u}_{w,i} \tag{4}$$

where  $\mathbf{u}_{w,i}$  is a column vector collecting the  $m_w$  warping DOFs  $u_{w,ij}$  of the  $i$ -th cross-section and  $\mathbf{M}(y,z)$  is a row vector containing the corresponding shape functions  $M_j(y,z)$ .

Finally, one-dimensional (1D) Lagrange polynomials  $N_i(x)$  associated to the  $n_w$  controlling points are used for the interpolation along the element axis. Field  $u_w(x,y,z)$ , thus, results as:

$$u_w(x,y,z) = \sum_{i=1}^{n_w} N_i(x)\mathbf{M}(y,z)\mathbf{u}_{w,i} \tag{5}$$

The compatible strain vector at the material point  $m$  collects the elongation  $\epsilon_{xx}(x,y,z)$  and the shear strains  $\gamma_{xy}(x,y,z)$  and  $\gamma_{xz}(x,y,z)$  in the cross-section plane, parallel to  $x-y$  and  $x-z$ , respectively. These result as:

$$\epsilon_m(x,y,z) = \mathbf{a}_s(y,z)\mathbf{e}(x) + \sum_{i=1}^{n_w} \left[ \frac{\partial N_i(x)}{\partial x} \mathbf{a}_w^x(y,z) + N_i(x)\mathbf{a}_w^{yz}(y,z) \right] \mathbf{u}_{w,i} \tag{6}$$

where  $\mathbf{e}(x)$  is the generalized section strain vector, collecting the normal strain  $\epsilon_0(x)$ , the flexural curvatures  $\chi_z(x)$  and  $\chi_y(x)$ , the torsional curvature  $\chi_x(x)$  and the shear strains  $\gamma_y(x)$  and  $\gamma_z(x)$ , while  $\mathbf{a}_w^x(y,z)$  and  $\mathbf{a}_w^{yz}(y,z)$  are two matrices with dimensions  $3 \times m_w$ , composed as follows:

$$\mathbf{a}_w^x(y,z) = \begin{bmatrix} \mathbf{M}(y,z) \\ \mathbf{0} \\ \mathbf{0} \end{bmatrix}, \quad \mathbf{a}_w^{yz}(y,z) = \begin{bmatrix} \mathbf{0} \\ \frac{\partial \mathbf{M}(y,z)}{\partial y} \\ \frac{\partial \mathbf{M}(y,z)}{\partial z} \end{bmatrix} \tag{7}$$



## 2.2 Element variational formulation

The equations governing the element state determination are derived from a modified Hu-Washizu variational principle, defined as function of four independent fields: the plane-section displacements, the strains and stresses and the additional warping displacement field  $u_w(x, y, z)$ . The functional is written as:

$$\Pi(\mathbf{u}_r, \varepsilon_m, \sigma_m, u_w) = \int_V \sigma_m^T [\varepsilon_m(\mathbf{u}_m) - \varepsilon_m] dV + \int_V \varepsilon_m^T \hat{\sigma}_m [\varepsilon_m] dV + \Pi_{\text{ext}} \quad (8)$$

where the dependency of the variables from  $x$ ,  $y$  and  $z$  is omitted. Vector  $\sigma_m(x, y, z)$  collects the actual material stresses work-conjugate to  $\varepsilon_m(x, y, z)$ , while  $\hat{\sigma}_m[\varepsilon_m(x, y, z)]$  represents the material stress vector associated to  $\varepsilon_m(x, y, z)$  that results from the material constitutive law.  $\Pi_{\text{ext}}$  is the external load potential and  $V$  indicates the element volume, being  $V = AL$ , with  $A$  the cross-section area.

Eq. (8) is modified [19] and the functional  $\Pi$  is expressed in terms of the generalized section displacements  $\mathbf{u}_s(x)$  and strains  $\mathbf{e}(x)$ . The stationarity of  $\Pi(\mathbf{u}_s, \mathbf{e}, \sigma_m, u_w)$  with respect to the four independent fields provides the following governing equations, as detailed in [19, 23]:

$$\begin{aligned} \mathbf{a}_g^T \mathbf{q} &= \mathbf{p} + \mathbf{p}_r \\ \sigma_m(x, y, z) &= \hat{\sigma}_m[\varepsilon_m(x, y, z)] \\ \mathbf{v} &= \int_0^L \mathbf{b}^T(x) \mathbf{e}(x) dx \\ \mathbf{p}_{w,i} &= \int_0^L \frac{\partial N_i(x)}{\partial x} \mathbf{s}_w^x(x) dx + \int_0^L N_i(x) \mathbf{s}_w^{yz}(x) dx \end{aligned} \quad (9)$$

Eq. (9)<sub>1</sub>, (9)<sub>2</sub> and (9)<sub>3</sub> are standard for a three-field mixed beam FE formulation. Eq. (9)<sub>1</sub> enforces the element equilibrium. This involves the transpose of  $\mathbf{a}_g$  and relates the twelve nodal forces  $\mathbf{p}$ , work-conjugate to  $\mathbf{u}$ , and the six element basic forces  $\mathbf{q}$ , work-conjugate to  $\mathbf{v}$ . Vector  $\mathbf{p}_r$  contains the element nodal reaction forces due the loads distributed along the element axis.

Eq. (9)<sub>2</sub> is the constitutive law governing the response of the material. The model discretizes the generic cross-section in a finite number of fibers, where the material response is evaluated and permits to use different constitutive models in case of composed steel-concrete or RC beams [36].

Eq. (9)<sub>3</sub> states the weak form of the element compatibility. This involves matrix  $\mathbf{b}^T(x)$ , that is the transpose of the equilibrium matrix [23] relating the generalized section stresses  $\mathbf{s}(x)$ , that are work-conjugate to  $\mathbf{e}(x)$ , to the basic forces  $\mathbf{q}$ , that is:

$$\mathbf{s}(x) = \mathbf{b}(x) \mathbf{q} + \mathbf{s}_q(x) \quad (10)$$

being  $\mathbf{s}_q(x)$  the contribution due to loads distributed along the element axis. The section stresses  $\mathbf{s}(x)$  are defined as:

$$\mathbf{s}(x) = \int_A \mathbf{a}_s^T(y, z) \sigma_m(x, y, z) dA \quad (11)$$

collecting the axial stress  $N(x)$ , the bending moments  $M_y(x)$  and  $M_z(x)$  about the  $y$ - and  $z$ -axis, respectively, the torsional moment  $M_x(x)$  and the generalized shear stresses  $T_y(x)$  and  $T_z(x)$  in the  $y$ - and  $z$ -direction, respectively.

Finally, Eq. (9)<sub>4</sub> enforces the section equilibrium condition related to the warping effects. Indeed, when the warping displacements are constrained at the element boundaries, an additional force field arises denoted with  $p_w(x, y, z)$ . Correspondingly, the vectors  $\mathbf{p}_{w,i}$ , with  $i = 1, \dots, n_w$ , are defined collecting the warping forces acting at the  $i$ -th section work-conjugate to  $\mathbf{u}_{w,i}$ . Hence, Eq. (9)<sub>4</sub> requires the forces  $\mathbf{p}_{w,i}$  to be in equilibrium with the generalized section stresses  $\mathbf{s}_w^x(x)$  and  $\mathbf{s}_w^{yz}(x)$  due to the warping. These result from the integral of the stresses as:

$$\mathbf{s}_w(x) = \begin{Bmatrix} \mathbf{s}_w^x(x) \\ \mathbf{s}_w^{yz}(x) \end{Bmatrix} = \begin{Bmatrix} \int_A \mathbf{a}_w^x(y, z)^T \sigma_m(x, y, z) dA \\ \int_A \mathbf{a}_w^{yz}(y, z)^T \sigma_m(x, y, z) dA \end{Bmatrix} \quad (12)$$

and play the role of bi-moments and bi-shears, classically introduced in thin-walled beam theories [18,37,38]. To be noted is that, according to the presented formulation, the generalized section stresses  $\mathbf{s}_w^x(x)$  and  $\mathbf{s}_w^{yz}(x)$  are each associated to the additional warping DOFs defined on the cross-section, whereas resultant components for bi-moments and bi-shears are defined in the classical thin-walled formulations.

## 2.3 Constitutive models

The material response of steel frame members is reproduced by adopting the J2 plasticity [31], while either this or the Giuffrè-Menegotto-Pinto model [39] is used for reinforcements in RC elements.

Concrete material response is described through the 3D constitutive model proposed by Di Re et al. [21] that is reviewed in the following. This extends the model proposed by Addessi et al. [40] by including the description of the unilateral effect typically of concrete-like materials, due to the crack opening and reclosure. A Drucker-Prager type plastic model [41] is coupled with a two-parameter isotropic damage model, where two scalar variables describe damage for prevailing tensile and compressive states, respectively. A modified version of this model was recently proposed for the analysis of masonry structures [42] yet considering a symmetric J2 plastic criterion.

To be noted is that the proposed FE model considers only three strain independent variables  $\varepsilon_m = \{\varepsilon_{xx}, \gamma_{xy}, \gamma_{xz}\}^T$  and three work-conjugate stress components  $\sigma_m = \{\sigma_{xx}, \tau_{xy}, \tau_{xz}\}^T$ . Hence, the adopted 3D model requires a condensation process to remove the strains and stresses  $\varepsilon_c = \{\varepsilon_{yy}, \varepsilon_{zz}, \gamma_{yz}\}^T$  and  $\sigma_c = \{\sigma_{yy}, \sigma_{zz}, \tau_{yz}\}^T$  and includes the 3D constitutive model in the beam formulation. The condensation procedure proposed in this work is described in Section 3.3. In the following, the model is recalled referring to



the six-component strain and stress vectors, namely  $\epsilon$  and  $\sigma$ . To simplify the notation, the dependency of the variables from  $x$ ,  $y$  and  $z$  is omitted.

The stress-strain relation is defined as:

$$\sigma = (1 - D)^2 \mathbf{C}(\epsilon - \epsilon^p) = (1 - D)^2 \mathbf{C}^e \epsilon^e \tag{13}$$

where  $\epsilon$ ,  $\epsilon^e$  and  $\epsilon^p$  are the total, elastic and plastic strain vectors, respectively,  $\sigma$  is the stress vector, and  $\mathbf{C}$  is the  $6 \times 6$  elastic isotropic matrix. The scalar variable  $D \in [0,1]$  governs the evolution of the degrading process, as detailed in the following.

The incremental constitutive relation is deduced by differentiating Eq. (13) and results as:

$$\dot{\sigma} = \left[ (1 - D)^2 \mathbf{C} - 2(1 - D) \mathbf{C} \epsilon^e \frac{\partial D}{\partial \epsilon} \right] \dot{\epsilon} = \mathbf{C}_t \dot{\epsilon} \tag{14}$$

with  $\mathbf{C}_t$  being the material tangent stiffness matrix and  $\mathbf{C}^{ep}$  the elasto-plastic tangent stiffness matrix.

The Drucker-Prager plasticity model with linear kinematic and isotropic hardening [41, 43] governs the evolution of the effective stresses  $\bar{\sigma} = \mathbf{C}(\epsilon - \epsilon^p)$ , with the plastic yield function defined as:

$$f(\bar{\sigma}, \bar{\zeta}, \alpha) = |\mathbf{P}\bar{\sigma} - \bar{\zeta}| - \sqrt{\frac{2}{3}}(\sigma_y + H_i \alpha) + \mu \mathbf{1}^T \bar{\sigma} \tag{15}$$

In Eq. (15), the column vector  $\mathbf{1}$  and the operator  $\mathbf{P}$  evaluates the first invariant and the deviatoric part of the effective stress  $\bar{\sigma}$ , respectively. The vector  $\bar{\zeta}$  is the kinematic effective back stress and  $\alpha$  the isotropic hardening variable.

These quantities and the plastic strains  $\epsilon^p$  evolve according to the variation of the plastic multiplier  $\lambda$  and the orientation of the vector  $\bar{\mathbf{n}} = (\mathbf{P}\bar{\sigma} - \bar{\zeta}) / |\mathbf{P}\bar{\sigma} - \bar{\zeta}|$  normal to the yield surface [21].

Considering the following relations [44]:

$$\sigma_y = \frac{2\sigma_c \sigma_t}{\sigma_c + \sigma_t}, \quad \mu = \sqrt{\frac{2}{3}} \left( \frac{\sigma_c - \sigma_t}{\sigma_c + \sigma_t} \right) \tag{16}$$

the material parameters required in Eq. (15) are the uniaxial tension and compression strengths,  $\sigma_t$  and  $\sigma_c$ , and the isotropic and kinematic hardening moduli,  $H_i$  and  $H_k$ .

The damage variable  $D$  depends on two different scalar quantities,  $D_t$  and  $D_c$ , measuring the damage for prevailing tensile and compressive states, respectively, with the condition  $D_t \geq D_c$ . The loading-unloading functions that govern their evolution are defined as:

$$f_h(Y_h, D_h) = Y_h - Y_{0h} - (a_h Y_h + k_h) D_h, \quad \text{with } h = t, c \tag{17}$$

where  $Y_{0h}$ ,  $k_h \geq 0$  and  $a_h \in [0,1]$  are material parameters, determining the damage strain threshold, the rate of damage growth and the slope of the softening branch, respectively. These can be determined from experimentally measured uniaxial stress-strain material response [21]. Thus,  $D$  results as the combination of  $D_t$  and  $D_c$ , in the form:

$$D = \alpha_t D_t + \alpha_c D_c \tag{18}$$

with  $\alpha_t$  and  $\alpha_c = 1 - \alpha_t$  being weighting coefficients, expressed for  $h = t, c$  as:

$$\alpha_h = \frac{\eta_h^2}{\eta_t^2 + \eta_c^2}, \quad \text{with } \eta_h = \frac{Y_h^e}{Y_{0h} + (a_h Y_h^e + k_h) D} \tag{19}$$

The scalar quantities  $Y_t$  and  $Y_c$  are equivalent strain measures, defined as:

$$Y_t = \sqrt{\sum_{i=1}^3 \langle e_i \rangle_+^2}, \quad Y_c = \sqrt{\sum_{i=1}^3 \langle e_i \rangle_-^2 - \beta \sum_{j=k} \langle e_j \rangle_- \langle e_k \rangle_-} \tag{20}$$

where the Macaulay brackets  $\langle \cdot \rangle_{+/-}$  evaluate the positive/negative part of the variable and:

$$e_i = (1 - 2\nu)\epsilon_i + \nu \sum_{j=1}^3 \epsilon_j, \quad \text{for } i = 1, 2, 3 \tag{21}$$

being  $\epsilon_i$  the principal total strains. Similarly,  $Y_t^e$  and  $Y_c^e$  are defined according to Eq. (20), but introducing the principal elastic strains  $\epsilon_i^e$ .  $\beta$  is a material parameter governing the shape of the limit function in compression.

Detailed discussion of the role played by each material parameter and their influence on the element response curve is reported in the previous work [21] and is not reported here for brevity.

Fig. 3a shows an example of cyclic uni-axial behavior, obtained by assuming for the material parameters the values in Table 1 and imposing the strain history depicted in Fig. 3b-i, while Fig. 3b-ii represents the corresponding evolution of the damage variables. Main steps of the two cycles performed in the loading path are indicated with capital letters.

As shown, the model can simulate the unilateral effects typical of concrete-like materials that is the crack closure-opening effect. Indeed, when the stress state switches from tension to compression (from step B to C and from step F to G), tensile damage is recovered and the response only depends on variable  $D_t$ . By contrast, when the stress state switches from compression to tension (from step D to E), compressive damage is not recovered and the response depends on both variables  $D_t$  and  $D_c$ .



Table 1. Material parameters for the cyclic uni-axial material response in Fig. 3.

$E$	$\nu$	$\sigma_t$	$\sigma_c$	$H_k$	$H_l$	$Y_{0t}$	$k_t$	$a_t$	$Y_{0c}$	$k_c$	$a_c$	$\beta$
30GPa	0.2	3.3MPa	30MPa	0.7E	0.001E	$7.2 \cdot 10^{-5}$	$2.0 \cdot 10^{-5}$	0.8	$3.6 \cdot 10^{-4}$	$5.0 \cdot 10^{-3}$	0.1	0.0

### 3. Solution Algorithm

The described beam FE formulation is implemented in a general FE analysis code. A step-by-step time discretization is adopted, as well as the iterative Newton-Raphson (N-R) algorithm for the solution of the governing nonlinear equations at each time step. The following sections describe the computational details of the solution algorithms developed to evaluate the model response.

#### 3.1 Element state determination

The global solution scheme of the FE code requires the element state determination, that is the computation of the element stiffness matrix  $\mathbf{k} = \partial \mathbf{p} / \partial \mathbf{u}$  and force vector  $\mathbf{p}$  at each N-R iteration. To this end, the governing equations are linearized and, after some manipulations (see Le Corvec [19]), the following set of equations is obtained:

$$\begin{aligned}
 \mathbf{k} \Delta \mathbf{u} &= \Delta \mathbf{p} \\
 \Delta \mathbf{s} &= \mathbf{k}_{ss} \Delta \mathbf{e} + \sum_{i=1}^{n_w} \left[ \frac{\partial N_i}{\partial X} \mathbf{k}_{sw}^x + N_i \mathbf{k}_{sw}^{yz} \right] \Delta \mathbf{u}_{w,i} \\
 \Delta \mathbf{v} &= \int_0^L \mathbf{b}^T \Delta \mathbf{e} dx \\
 \Delta \mathbf{p}_{w,i} &= \int_0^L \frac{\partial N_i}{\partial X} \Delta \mathbf{s}_w^x dx + \int_0^L N_i \Delta \mathbf{s}_w^{yz} dx
 \end{aligned} \tag{22}$$

together with the linearized form of the section equilibrium equation, resulting as:

$$\Delta \mathbf{s} = \mathbf{b} \Delta \mathbf{q}, \quad \text{with} \quad \Delta \mathbf{q} = \mathbf{f}^{-1} \Delta \mathbf{v} \tag{23}$$

where  $\mathbf{f}$  is the element basic flexibility matrix governing the incremental relation between  $\mathbf{q}$  and  $\mathbf{v}$ . Symbol  $\Delta$  denotes the increment of the variable at each iteration.

Eq. (22)<sub>2</sub> is the linearized section constitutive law. This is coupled with the constitutive laws governing the evolution of the warping section stresses in Eq. (12), whose linearized forms result in:

$$\Delta \mathbf{s}_w^x = \mathbf{k}_{ws}^x \Delta \mathbf{e} + \sum_{i=1}^{n_w} \left[ \frac{\partial N_i}{\partial X} \mathbf{k}_{ww}^x + N_i \mathbf{k}_{ww}^{xy} \right] \Delta \mathbf{u}_{w,i}, \quad \Delta \mathbf{s}_w^{yz} = \mathbf{k}_{ws}^{yz} \Delta \mathbf{e} + \sum_{i=1}^{n_w} \left[ \frac{\partial N_i}{\partial X} \mathbf{k}_{ww}^{yz} + N_i \mathbf{k}_{ww}^{yz} \right] \Delta \mathbf{u}_{w,i} \tag{24}$$

Eqs. (22)<sub>2</sub> and (24) involve two contributions: the first depends on the standard strain vector  $\mathbf{e}$ , compatible with the cross-section motions associated to plane-section assumption, and the second on the section strains due to the warping. The standard section stiffness matrix  $\mathbf{k}_{ss}$  and the additional eight section warping stiffness matrices  $\mathbf{k}_{sw}^x$ ,  $\mathbf{k}_{sw}^{yz}$ ,  $\mathbf{k}_{ws}^x$ ,  $\mathbf{k}_{ws}^{yz}$ ,  $\mathbf{k}_{ww}^x$ ,  $\mathbf{k}_{ww}^{yz}$ ,  $\mathbf{k}_{ww}^{xy}$  and  $\mathbf{k}_{ww}^{yz}$  are defined as:

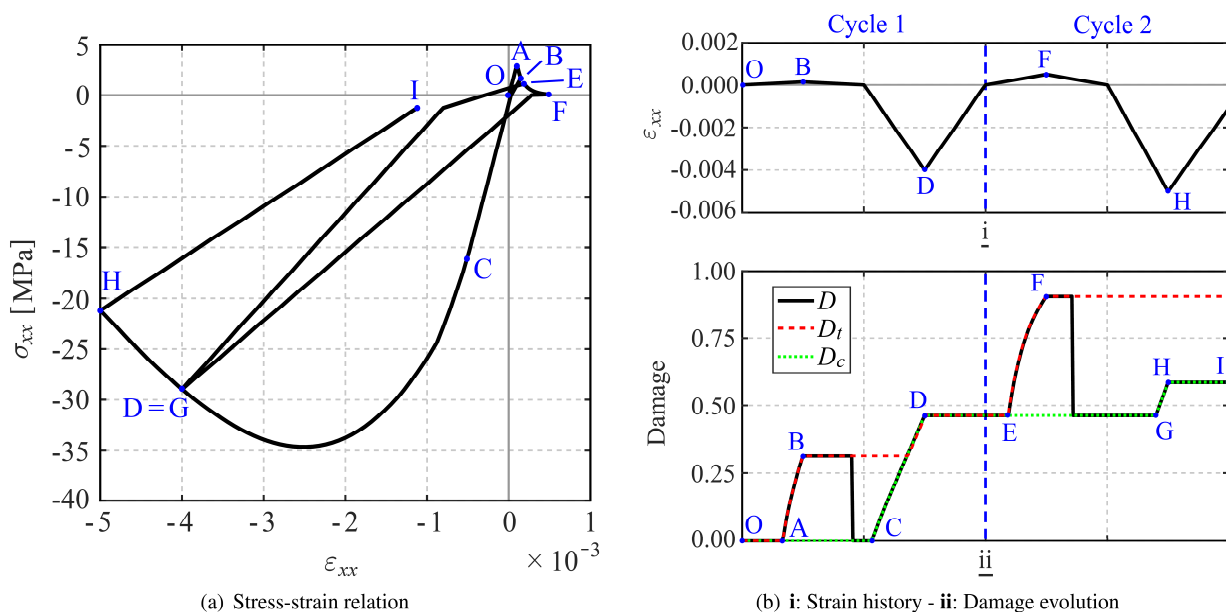


Fig. 3. Cyclic uni-axial behavior under imposed strain history for the proposed damage model.



$$\begin{aligned}
 \mathbf{k}_{ss} &= \int_A \mathbf{a}_s^T \mathbf{k}_m \mathbf{a}_s dA \\
 \mathbf{k}_{sw}^{x/yz} &= \left\{ \int_A \mathbf{a}_s^T \mathbf{k}_m \mathbf{a}_w^{x/yz} dA \right\} \Gamma, & \mathbf{k}_{ws}^{x/yz} &= \Gamma^T \left\{ \int_A (\mathbf{a}_w^{x/yz})^T \mathbf{k}_m \mathbf{a}_s dA \right\} \\
 \mathbf{k}_{ww}^{x/yz} &= \Gamma^T \left\{ \int_A (\mathbf{a}_w^{x/yz})^T \mathbf{k}_m \mathbf{a}_w^{x/yz} dA \right\} \Gamma + \Psi, & \mathbf{k}_{ww}^{xy/yx} &= \Gamma^T \left\{ \int_A (\mathbf{a}_w^{x/yz})^T \mathbf{k}_m \mathbf{a}_w^{yz/x} dA \right\} \Gamma + \Psi
 \end{aligned} \tag{25}$$

where  $\Gamma$  and  $\Psi$  are the projection and correction matrix, defined subsequently, and  $\mathbf{k}_m$  is the consistent material stiffness matrix, governing the incremental material stress-strain relation, whose linearized form results as:

$$\Delta \sigma_m = \mathbf{k}_m \Delta \varepsilon_m \tag{26}$$

The compact form of Eq. (22)<sub>4</sub> is obtained by collecting all the warping DOFs used in Eq. (5) in a single vector  $\mathbf{u}_w$ , i.e.:

$$\mathbf{u}_w = \{ \mathbf{u}_{w,1}^T \quad \mathbf{u}_{w,2}^T \quad \dots \quad \mathbf{u}_{w,i}^T \quad \dots \quad \mathbf{u}_{w,n_w}^T \}^T \tag{27}$$

and the warping forces  $\mathbf{p}_{w,i}$  in the work-conjugate vector  $\mathbf{p}_w$ . Hence, Eq. (22)<sub>4</sub> becomes:

$$\Delta \mathbf{p}_w = \mathbf{b}_{ws} \Delta \mathbf{q} + \mathbf{k}_{ww} \Delta \mathbf{u}_w \tag{28}$$

where  $\Delta \mathbf{u}_w$  and  $\Delta \mathbf{p}_w$  are increments of  $\mathbf{u}_w$  and  $\mathbf{p}_w$ , respectively. Matrices  $\mathbf{k}_{ww}$  and  $\mathbf{b}_{ws}$  in Eq. (28) are defined as:

$$\mathbf{k}_{ww} = \begin{bmatrix} \mathbf{k}_{w,1,1} & \dots & \mathbf{k}_{w,1,n_w} \\ \vdots & \ddots & \vdots \\ \mathbf{k}_{w,n_w,1} & \dots & \mathbf{k}_{w,n_w,n_w} \end{bmatrix}, \quad \mathbf{b}_{ws} = \begin{bmatrix} \mathbf{b}_{ws,1} \\ \vdots \\ \mathbf{b}_{ws,n_w} \end{bmatrix} \tag{29}$$

where:

$$\begin{aligned}
 \mathbf{k}_{w,i,n} &= \int_0^L \mathbf{k}_{ww,i,n} - \mathbf{k}_{ws,i} \mathbf{k}_{ss}^{-1} \mathbf{k}_{sw,n} dx, & \mathbf{b}_{ws,i} &= \int_0^L \mathbf{k}_{ws,i} \mathbf{k}_{ss}^{-1} \mathbf{b} dx \\
 \mathbf{k}_{ws,i} &= \frac{\partial N_i}{\partial X} \mathbf{k}_{ws}^x + N_i \mathbf{k}_{ws}^{yz}, & \mathbf{k}_{sw,i} &= \frac{\partial N_i}{\partial X} \mathbf{k}_{sw}^x + N_i \mathbf{k}_{sw}^{yz} \\
 \mathbf{k}_{ww,i,n} &= \frac{\partial N_i}{\partial X} \left[ \frac{\partial N_n}{\partial X} \mathbf{k}_{ww}^x + N_n \mathbf{k}_{ww}^{xy} \right] + N_i \left[ \frac{\partial N_n}{\partial X} \mathbf{k}_{ww}^{yx} + N_n \mathbf{k}_{ww}^{yz} \right]
 \end{aligned} \tag{30}$$

Manipulating the governing equations gives the element flexibility matrix  $\mathbf{f}$  as the sum of two contributions, i.e.:

$$\mathbf{f} = \mathbf{f}_s + \mathbf{f}_w = \int_0^L \mathbf{b}^T \mathbf{k}_{ss}^{-1} \mathbf{b} dx + \mathbf{b}_{sw} \mathbf{k}_{ww}^{-1} \mathbf{b}_{ws} \tag{31}$$

where  $\mathbf{f}_s$  is the standard flexibility matrix for the beam force formulation and  $\mathbf{f}_w$  is the contribution due to the warping effects. Hence, the consistent element global stiffness matrix  $\mathbf{k}$  results as:

$$\mathbf{k} = \mathbf{a}_g^T \mathbf{f}^{-1} \mathbf{a}_g \tag{32}$$

When the material stiffness matrix  $\mathbf{k}_m$  is symmetric,  $\mathbf{k}_{ww}$  is symmetric as well and  $\mathbf{b}_{sw} = \mathbf{b}_{ws}^T$ . Hence,  $\mathbf{f}_s$ ,  $\mathbf{f}_w$  and  $\mathbf{k}$  are symmetric, as well. Conversely, if  $\mathbf{k}_m$  is non-symmetric,  $\mathbf{k}_{ww}$  is non-symmetric and  $\mathbf{b}_{sw} \neq \mathbf{b}_{ws}^T$ . This is the case of the plastic-damage model adopted for concrete in this work, as it is based on the Drucker-Prager plasticity criterion. In this situation, the following additional expressions are required:

$$\mathbf{b}_{sw} = [ \mathbf{b}_{sw,1} \quad \dots \quad \mathbf{b}_{sw,n_w} ], \quad \text{with} \quad \mathbf{b}_{sw,i} = \int_0^L \mathbf{b}^T \mathbf{k}_{ss}^{-1} \mathbf{k}_{sw,i} dx \tag{33}$$

The plane-section and warping displacement fields in Eq. (3) are assumed to be orthogonal. The definition of redundant displacement fields makes matrix  $\mathbf{k}_{ww}$  in Eq. (31) to be singular. Hence, the plane-section displacement fields have to be eliminated from the displacement field  $u_w$  by modifying the interpolation functions  $M_j$  in Eq. (4). The matrices  $\Gamma$  and  $\Psi$  in Eqs. (25) accomplish this task, ensuring the non-singularity of matrix  $\mathbf{k}_{ww}$ . This paper proposes a modification of the definition of  $\Gamma$  and  $\Psi$ , with respect to those adopted by Le Corvec [19], that improves the numerical stability. Being  $\mathbf{V}$  the matrix containing the average value and the first moments of the shape functions over the cross section, i.e.:

$$\mathbf{V} = \int_A \begin{bmatrix} 1 \\ y \\ z \end{bmatrix} \mathbf{M} dA \tag{34}$$

the projection and correction matrices are defined as:

$$\Gamma = \mathbf{I}(m_w) - \Psi, \quad \Psi = \hat{\mathbf{V}}^T \hat{\mathbf{V}} \tag{35}$$

where  $\mathbf{I}(m_w)$  is the  $m_w \times m_w$  identity matrix and  $\hat{\mathbf{V}}$  is the orthogonal matrix, resulting from the Gram-Schmidt orthonormalization [45] of  $\mathbf{V}$ , performed assuming as linear independent vectors the rows of  $\mathbf{V}$ .



Depending on the boundary conditions, warping displacement constraints can be applied at the element boundaries. This study considers only totally free or fully restrained warping displacements, by imposing the conditions  $p_{w,ij} = 0$  or  $u_{w,ij} = 0$ , respectively. Thus, mixed boundary conditions are not considered. Consequently, Eq. (28) is split in the part associated to the free and that associated to the restrained DOFs, denoted with subscript 'f' and 'r', respectively:

$$\begin{Bmatrix} \Delta \mathbf{p}_{w,f} \\ \Delta \mathbf{p}_{w,r} \end{Bmatrix} = \begin{Bmatrix} \mathbf{b}_{ws,f} \\ \mathbf{b}_{ws,r} \end{Bmatrix} \Delta \mathbf{q} + \begin{Bmatrix} \mathbf{k}_{ww,ff} & \mathbf{k}_{ww,fr} \\ \mathbf{k}_{ww,rf} & \mathbf{k}_{ww,rr} \end{Bmatrix} \begin{Bmatrix} \Delta \mathbf{u}_{w,f} \\ \mathbf{0} \end{Bmatrix} \quad (36)$$

Moreover, each free warping DOF in  $\mathbf{u}_{w,f}$  and the work-conjugate force in  $\mathbf{p}_{w,f}$  can be treated in a different way. Two cases are distinguished:

1. The warping DOF is considered as external variable and added to the standard twelve DOFs.
2. The warping DOF is considered as internal variable and is condensed out with the evaluation of the element flexibility matrix.

Usually, all the warping DOFs belonging to the same cross-section are considered as either internal or external variables, although there is no limitation in this choice. When all the warping DOFs are considered as internal, only the standard twelve DOFs result as actual independent element variables, otherwise the first set of Eq. (36) is modified by splitting the vector  $\mathbf{u}_{w,f}$  into the local and global DOFs  $\mathbf{u}_{w,l}$  and  $\mathbf{u}_{w,g}$ , respectively:

$$\begin{Bmatrix} \Delta \mathbf{p}_{w,l} \\ \Delta \mathbf{p}_{w,g} \end{Bmatrix} = \begin{Bmatrix} \mathbf{b}_{ws,l} \\ \mathbf{b}_{ws,g} \end{Bmatrix} \Delta \mathbf{q} + \begin{Bmatrix} \mathbf{k}_{ww,ll} & \mathbf{k}_{ww,lg} \\ \mathbf{k}_{ww,gl} & \mathbf{k}_{ww,gg} \end{Bmatrix} \begin{Bmatrix} \Delta \mathbf{u}_{w,l} \\ \Delta \mathbf{u}_{w,g} \end{Bmatrix} \quad (37)$$

The global part  $\mathbf{u}_{w,g}$  is added to the standard twelve element DOFs and, thus, Eq. (2) becomes:

$$\Delta \tilde{\mathbf{v}} = \begin{Bmatrix} \Delta \mathbf{v} \\ \Delta \mathbf{u}_{w,g} \end{Bmatrix} = \begin{bmatrix} \mathbf{a}_g & \mathbf{0} \\ \mathbf{0} & \mathbf{I} \end{bmatrix} \begin{Bmatrix} \Delta \mathbf{u} \\ \Delta \mathbf{u}_{w,g} \end{Bmatrix} = \tilde{\mathbf{a}}_g \Delta \tilde{\mathbf{u}} \quad (38)$$

with  $\mathbf{I}$  a properly sized identity matrix. Similarly, the linearized form of the second of Eq. (23) becomes:

$$\Delta \tilde{\mathbf{v}} = \begin{Bmatrix} \Delta \mathbf{v} \\ \Delta \mathbf{u}_{w,g} \end{Bmatrix} = \begin{bmatrix} \mathbf{f}_{qq} & \mathbf{f}_{qw} \\ \mathbf{f}_{wq} & \mathbf{f}_{ww} \end{bmatrix} \begin{Bmatrix} \Delta \mathbf{q} \\ \Delta \mathbf{p}_{w,g} \end{Bmatrix} = \tilde{\mathbf{f}} \Delta \tilde{\mathbf{q}} \quad (39)$$

with the expressions of  $\mathbf{f}_{qq}$ ,  $\mathbf{f}_{qw}$ ,  $\mathbf{f}_{wq}$  and  $\mathbf{f}_{ww}$  given by Le Corvec [19]. Finally, the global element stiffness matrix in Eq. (32) and force vector in Eq. (9)<sub>1</sub> that account for the global warping DOFs result as:

$$\tilde{\mathbf{k}} = \tilde{\mathbf{a}}_g^T \tilde{\mathbf{f}}^{-1} \tilde{\mathbf{a}}_g, \quad \tilde{\mathbf{p}} = \tilde{\mathbf{a}}_g^T \tilde{\mathbf{q}} - \tilde{\mathbf{p}}_r \quad (40)$$

with  $\tilde{\mathbf{p}}_r = (\mathbf{p}_r^T \quad \mathbf{0}^T)^T$  and Eq. (22)<sub>1</sub> becoming:

$$\tilde{\mathbf{k}} \Delta \tilde{\mathbf{u}} = \Delta \tilde{\mathbf{p}} \quad (41)$$

The definition of the warping DOFs as global quantities is often required to enforce the continuity of the warping displacement field  $u_w(x,y,z)$ , e.g., when more than one FE discretize a single structural element or in case of frames made by assembling multiple members with different axis directions [23]. Indeed, when the coinciding end cross-sections of two contiguous elements adopt the same warping interpolation scheme, i.e., the same number and location of warping DOFs, their warping profiles coincide if these DOFs are treated as global quantities. By contrast, for  $\mathbf{u}_{w,r}$ , it is not necessary to distinguish between internal and global DOFs, as the restrained DOFs can always be treated as internal variables. In this case, the warping displacement field continuity is automatically ensured by the condition  $u_{w,ij} = 0$  imposed at both the coinciding end cross-sections.

It is worth mentioning that the recent work by the authors [23] presents a general method to derive the element governing equations from the stationarity of an extended four-field Lagrangian functional, which also accounts for dynamic inertia effects. In this case, warping DOFs are always treated as external variables and warping displacement continuity between elements is automatically ensured. However, in this paper, the equivalent approach as that adopted by Le Corvec [19] is followed, as described above.

Relying on the above considerations, the element state determination procedure results as summarized in Table 2, where the superscripts 'k' and 'k+1' denote the previous and current N-R iteration, respectively. The algorithm is the generalization of that developed for a standard force-based beam FE [28, 30]. For a given set of total and incremental displacements  $\mathbf{u}$ ,  $\Delta \mathbf{u}$ ,  $\mathbf{u}_{w,g}$  and  $\Delta \mathbf{u}_{w,g}$  (step 1), the algorithm evaluates the increment of the basic element forces  $\Delta \mathbf{q}$  from the increment of the basic element displacements  $\Delta \tilde{\mathbf{v}}$  (steps 2 and 3). The updated  $\mathbf{q}$  are, then, used in a nested iterative procedure (step 4), required to enforce both element equilibrium and compatibility conditions, as usual in force-based beam FEs. At the end of this procedure, after the initialization of some variables (step 5), steps 6 to 8 perform the updating of the warping quantities. Indeed, the first set of Eq. (37) gives the increment of the free warping DOF displacements  $\Delta \mathbf{u}_{w,l}$ . Together with the given quantities  $\mathbf{u}_{w,g}$ , these can be used in the second set of Eq. (36) to determine the increment of the warping forces  $\Delta \mathbf{p}_{w,r}$  for the restrained DOFs. Hence, the section strains  $\mathbf{e}$  are updated to comply with the section stresses  $\mathbf{s}$  that are in equilibrium with the last basic element forces [30] (steps 9 and 10). Finally, the element stiffness matrix and nodal forces are evaluated.





Table 2. Element state determination.

1)	$\mathbf{u}^{k+1}, \Delta \mathbf{u}^{k+1}, \mathbf{u}_{w,g}^{k+1}$ and $\Delta \mathbf{u}_{w,g}^{k+1}$ given
2)	$\Delta \tilde{\mathbf{v}}^{k+1} = \tilde{\mathbf{a}}_g \Delta \tilde{\mathbf{u}}^{k+1}$
3)	$\Delta \tilde{\mathbf{q}}^{k+1} = (\tilde{\mathbf{f}}^k)^{-1} \Delta \tilde{\mathbf{v}}^{k+1} \rightarrow \tilde{\mathbf{q}}^{k+1} = \tilde{\mathbf{q}}^k + \Delta \tilde{\mathbf{q}}^{k+1}$
4)	Element nested procedure in Table 3 to update the element state (converged iteration $l + 1$ )
5)	Current state $k + 1$ set equal to the converged state $l + 1$ and: $\hat{\mathbf{u}}_{w,l}^{k+1} = \mathbf{u}_{w,l}^{l+1}, \hat{\mathbf{p}}_{w,r}^{k+1} = \mathbf{p}_{w,r}^{l+1}, \hat{\mathbf{e}}^{k+1} = \mathbf{e}^{l+1}, \hat{\mathbf{s}}^{k+1} = \mathbf{s}^{l+1}$
6)	$\Delta \mathbf{u}_{w,l}^{k+1} = (\mathbf{k}_{w,w,\Pi}^{k+1})^{-1} [\hat{\mathbf{p}}_{w,l}^{k+1} - \mathbf{b}_{w,r}^{k+1} \Delta \tilde{\mathbf{q}}^{k+1} - \mathbf{k}_{w,w,lg}^{k+1} \Delta \mathbf{u}_{w,g}^{k+1}]$
7)	$\mathbf{u}_{w,l}^{k+1} = \hat{\mathbf{u}}_{w,l}^{k+1} + \Delta \mathbf{u}_{w,l}^{k+1}$
8)	$\hat{\mathbf{p}}_{w,r}^{k+1} = \hat{\mathbf{p}}_{w,r}^{k+1} + \mathbf{b}_{w,r}^{k+1} \Delta \tilde{\mathbf{q}}^{k+1} + \mathbf{k}_{w,w,rf}^{k+1} \Delta \mathbf{u}_{w,f}^{k+1}$
9)	$\mathbf{s}^{k+1} = \mathbf{b} \mathbf{q}^{k+1} + \mathbf{s}_q^{k+1}$
10)	$\mathbf{e}^{k+1} = \hat{\mathbf{e}}^{k+1} + (\mathbf{k}_{ss}^{k+1})^{-1} \left[ \mathbf{s}^{k+1} - \hat{\mathbf{s}}^{k+1} - \sum_{i=1}^n \mathbf{k}_{sw,i}^{k+1} \Delta \mathbf{u}_{w,i}^{k+1} \right]$
11)	$\tilde{\mathbf{k}}^{k+1} = \tilde{\mathbf{a}}_g^T (\tilde{\mathbf{f}}^{k+1})^{-1} \tilde{\mathbf{a}}_g$ and $\tilde{\mathbf{p}}^{k+1} = \tilde{\mathbf{a}}_g^T \tilde{\mathbf{q}}^{k+1} - \tilde{\mathbf{p}}_r^{k+1}$

The details of the nested iterative procedure are summarized in Table 3, where the superscript 'l' and 'l+1' denote the previous and current internal iteration. In the described beam formulation, the section response is governed by three equations: (22)<sub>2</sub> and (24)<sub>1-2</sub>, expressed in the compact form of Eq. (28). Hence, for given basic element forces  $\mathbf{q}$  the increment of the warping displacements  $\mathbf{u}_w$  needs to be first determined in steps 1 and 2 and then used in the evaluation of the section strains  $\mathbf{e}$  in step 3. This observation gives rise to the similar updating performed in step 10 of Table 2.

Step 4 performs the section state determination, that is the evaluation of the cross-section response for the updated section strains  $\mathbf{e}$ , in terms of section stresses and stiffness matrices. This is described in the following Section 3.2.

After evaluating the section response, in steps 5 and 6, the element warping stiffness matrices and forces are computed. Hence, as usual in force-based FEs, the equilibrated section stresses  $\mathbf{s}$  are evaluated on the basis of the current increment of the element basic forces  $\mathbf{q}$  (step 7) and are used to determine the increment of the section strains  $\mathbf{e}$  (step 10). These are, then, integrated along the element axis and compared with the given element basic displacements  $\mathbf{v}$  (step 11). However, similarly to step 3, the residual of the warping displacements  $\bar{\mathbf{u}}_w$  is required in step 10 for determining the residual of the section strains.  $\bar{\mathbf{u}}_w$  derives from the residual  $\bar{\mathbf{p}}_w$  of the warping forces, determined in steps 8 and 9 by considering that zero values are expected for the components related to the free local DOFs. Finally, the resulting residual is used to correct the basic element forces  $\mathbf{q}$  for the next iteration (steps 12 and 13).

The non-iterative version of this algorithm results by simply setting the maximum number of iterations  $I_{max} = 1$ , as in the algorithm proposed in [30] for the standard element. In this way, the residual element basic displacements are included in the basic element forces, which are, then, used to determine the end forces  $\mathbf{p}$  in the global reference system at the end of the element state determination in Table 2. Hence, the error associated to the element residual forces is included in the equilibrium equations solved at the global level and is iteratively driven to zero. The main advantages of the non-iterative approach are discussed in [46], where it was first proposed for standard elements. Moreover, this results particularly convenient when softening occurs at the element level. Indeed, the adoption of non-iterative algorithm can help in by-passing convergence issues at the local level, as it is possible to count on the better path-following performance of the global solution strategy. To be noted is that small issues can occur in situations where local element residual is relevant. However, these are usually limited to a reduction of the convergence rate.

To perform the integrals along the element axis, the Gauss-Lobatto integration scheme is adopted in this work, as this places quadrature points at the ends of the beams, where stresses often attain their maximum values, e.g for frames subjected to horizontal loadings, but any integration scheme can be in general utilized. Hence, the evaluation of the section quantities is performed at the quadrature points, whose number and location are completely independent from those used for the warping interpolation. The quadrature integration rule, properly modified, is also exploited to regularize the response of the beam element that is to avoid mesh dependency of the results and localization issues for softening material responses. In force-based and mixed beam FEs, strain-damage localization occurs at the quadrature cross-section where strains reach their maximum values and is affected by the weighting length associated to them by the quadrature rule. Hence, the approach proposed by Addessi et al. [47] is used, that is the weighting length associated to the maximum stressed quadrature cross-section is controlled.

### 3.2 Fiber section model

For a force-based FE the section state determination consists in computing the resisting generalized section stresses  $\mathbf{s}$  and the tangent section stiffness matrix  $\mathbf{k}_{ss}$  under given generalized section strains  $\mathbf{e}$ . For the proposed mixed element with section warping, this evaluation also depends on the warping displacement field  $u_w$  and also provides the generalized stresses  $\mathbf{s}_w^x$  and  $\mathbf{s}_w^{yz}$  and the warping stiffness matrices  $\mathbf{k}_{sw}^{x/yz}, \mathbf{k}_{ws}^{x/yz}, \mathbf{k}_{ww}^{x/yz}, \mathbf{k}_{ww}^{xy/yz}$ .



Table 3. Element nested iterative procedure.

---

Initialization:  
 State  $l = 0$  set equal to the state  $k$  (Table 2) and:  
 $\Delta \mathbf{q}^{l+1} = \Delta \mathbf{q}^{k+1}$ ,  $\mathbf{q}^{l+1} = \mathbf{q}^{k+1}$ ,  $\Delta \mathbf{u}_{w,g}^{l+1} = \Delta \mathbf{u}_{w,g}^{k+1}$ ,  $\mathbf{u}_{w,g}^{l+1} = \mathbf{u}_{w,g}^{k+1}$ ,  $\mathbf{s}_q^{l+1} = \mathbf{s}_q^{k+1}$  and  $\bar{\mathbf{p}}_{w,f}^l = \mathbf{0}$

---

- 1)  $\Delta \mathbf{u}_{w,l}^{l+1} = (\mathbf{k}_{ww,ll}^l)^{-1} [\bar{\mathbf{p}}_{w,l}^l - \mathbf{b}_{ws,l}^l \Delta \mathbf{q}^{l+1} - \mathbf{k}_{ww,lg}^l \Delta \mathbf{u}_{w,g}^{l+1}]$
- 2)  $\mathbf{u}_{w,l}^{l+1} = \mathbf{u}_{w,l}^l + \Delta \mathbf{u}_{w,l}^{l+1}$
- 3)  $\mathbf{e}^{l+1} = \mathbf{e}^l + (\mathbf{k}_{ss}^l)^{-1} \left[ \mathbf{b} \Delta \mathbf{q}^{l+1} - \sum_{i=1}^{n_s} \mathbf{k}_{sw,i}^l \Delta \mathbf{u}_{w,i}^{l+1} \right]$
- 4) Section state determination in Table 4:  
 $\mathbf{e}^{l+1}$ ,  $\mathbf{u}_w^{l+1} \rightarrow \mathbf{s}^{l+1}$ ,  $\mathbf{k}_{ss}^{l+1}$ ,  $\mathbf{s}_w^{x,l+1}$ ,  $\mathbf{s}_w^{yz,l+1}$ ,  $\mathbf{k}_{ws}^{x/yz,l+1}$ ,  $\mathbf{k}_{ww}^{x/yz,l+1}$ , etc.
- 5) Evaluation of  $\mathbf{b}_{sw}^{l+1}$ ,  $\mathbf{b}_{ws}^{l+1}$  and  $\mathbf{k}_{ww}^{l+1}$  from Eqs. (29) to (33)
- 6)  $\mathbf{p}_{w,i}^{l+1} = \int_0^L \left[ \frac{\partial N_i}{\partial x} \mathbf{s}_w^{x,l+1} + N_i \mathbf{s}_w^{yz,l+1} \right] dx \rightarrow \mathbf{p}_w^{l+1} = (\mathbf{p}_{w,1}^{l+1}, \mathbf{p}_{w,2}^{l+1}, \dots, \mathbf{p}_{w,n_s}^{l+1})^T$
- 7)  $\bar{\mathbf{s}}^{l+1} = \mathbf{b} \mathbf{q}^{l+1} + \mathbf{s}_q^{l+1} - \mathbf{s}^{l+1}$
- 8)  $\bar{\mathbf{p}}_{ws,i}^{l+1} = \int_0^L \mathbf{k}_{ws,i}^{l+1} (\mathbf{k}_{ss}^{l+1})^{-1} \bar{\mathbf{s}}^{l+1} dx \rightarrow \bar{\mathbf{p}}_{ws}^{l+1} = (\bar{\mathbf{p}}_{ws,1}^{l+1}, \bar{\mathbf{p}}_{ws,2}^{l+1}, \dots, \bar{\mathbf{p}}_{ws,n_s}^{l+1})^T$
- 9)  $\bar{\mathbf{p}}_{w,f}^{l+1} = -(\mathbf{p}_{w,f}^{l+1} + \bar{\mathbf{p}}_{ws,f}^{l+1})$
- 10)  $\bar{\mathbf{u}}_{w,l}^{l+1} = (\mathbf{k}_{ww,ll}^{l+1})^{-1} \bar{\mathbf{p}}_{w,l}^{l+1} \rightarrow \bar{\mathbf{e}}^{l+1} = (\mathbf{k}_{ss}^{l+1})^{-1} \left[ \bar{\mathbf{s}}^{l+1} - \sum_{n=1}^{n_s} \mathbf{k}_{sw,n}^{l+1} \bar{\mathbf{u}}_{w,n}^{l+1} \right]$
- 11)  $\bar{\mathbf{v}}^{l+1} = \mathbf{a}_g \mathbf{u}^{k+1} - \int_0^L \mathbf{b}^T (\mathbf{e}^{l+1} + \bar{\mathbf{e}}^{l+1}) dx$  and  $\bar{\mathbf{f}}^{l+1}$  as in Eq. (39)
- 12)  $\Delta \mathbf{q}^{l+1} = \left[ \mathbf{f}_{qq}^{l+1} - \mathbf{f}_{qw}^{l+1} (\mathbf{f}_{ww}^{l+1})^{-1} \mathbf{f}_{wq}^{l+1} \right]^{-1} \bar{\mathbf{v}}^{l+1}$
- 13)  $\mathbf{q}^{l+1} = \begin{pmatrix} \mathbf{q}^{l+1} + \Delta \mathbf{q}^{l+1} \\ \bar{\mathbf{p}}_{w,g}^{l+1} \end{pmatrix}$
- 14) The following residual internal energy is evaluated:  
 $\bar{W}^{l+1} = \int_0^L (\bar{\mathbf{s}}^{l+1})^T \bar{\mathbf{e}}^{l+1} dx + (\bar{\mathbf{p}}_w^{l+1})^T \bar{\mathbf{u}}_w^{l+1}$   
 If  $\bar{W}^{l+1} < tolerance$  or  $l \geq l_{max} \rightarrow EXIT$ ,  
 otherwise  $\rightarrow GO TO step 1)$

---

Table 4. Section state determination.

---

- 1)  $\mathbf{e}^{l+1}$  and  $\mathbf{u}_w^{l+1}$  given
- 2)  $\epsilon_m^{l+1} = \mathbf{a}_s \mathbf{e}^{l+1} + \sum_{i=1}^{n_s} \left[ \frac{\partial N_i}{\partial x} \mathbf{a}_w^x + N_i \mathbf{a}_w^{yz} \right] \mathbf{u}_{w,i}^{l+1}$
- 3) Material state determination and static condensation of  $\sigma_c$  in Table 5 and Table 6:  
 $\epsilon_m^{l+1} \rightarrow \sigma_m^{l+1} = \sigma_m[\epsilon_m^{l+1}]$  and  $\mathbf{k}_m^{l+1} = \mathbf{k}_m[\epsilon_m^{l+1}]$
- 4)  $\mathbf{s}^{l+1} = \int_A \mathbf{a}_s^T \sigma_m^{l+1} dA$  and  $\mathbf{k}_{ss}^{l+1} = \int_A \mathbf{a}_s^T \mathbf{k}_m^{l+1} \mathbf{a}_s dA$
- 5)  $\mathbf{s}_w^{x,l+1} = \int_A (\mathbf{a}_w^x)^T \sigma_m^{l+1} dA$ ,  $\mathbf{s}_w^{yz,l+1} = \int_A (\mathbf{a}_w^{yz})^T \sigma_m^{l+1} dA$   
 $\mathbf{k}_{sw}^{x/yz,l+1}$ ,  $\mathbf{k}_{ws}^{x/yz,l+1}$ ,  $\mathbf{k}_{ww}^{x/yz,l+1}$ ,  $\mathbf{k}_{ww}^{xy/yz,l+1}$  Eqs. (25)

---

Table 4 summarizes the main steps of the corresponding numerical procedure. Known the updated section strains  $\mathbf{e}$  and warping displacements  $\mathbf{u}_w$  (step 1), the compatible material strains  $\epsilon_m$  (step 2) are evaluated and used to perform the material state determination in step 3, that is the evaluation of the material response in terms of stresses and stiffness. This procedure is described in the following Section 3.3 for the 3D plastic-damage constitutive model used for concrete material, but similar considerations hold for any 3D material relationship. Finally, after material stresses and stiffness matrices are computed, these



are integrated over the cross-section to obtain the corresponding generalized section quantities (steps 4 and 5).

To evaluate the integrals over the cross-section area, the proposed model adopts a fiber discretization [35]. For a nonlinear material response, Kostic et al. [36] demonstrated that the midpoint rule is the best scheme in terms of accuracy of the solution and minimum number of fibers, i.e., computational burden. This means that each rectangular patch composing the cross-section is discretized with a uniform (equally spaced) grid of points and each point is located at the midpoint of the associated weighting area.

### 3.3 Condensation and solution procedure for the plastic-damage model

The material state determination consists in computing the stresses  $\sigma_m$  and the tangent stiffness matrix  $\mathbf{k}_m$  for the given strains  $\epsilon_m$  at each point used to perform the numerical integration over the cross-section. However, condensation of in-plane components  $\epsilon_c = (\epsilon_{yy}, \epsilon_{zz}, \gamma_{yz})^T$  and  $\sigma_c = (\sigma_{yy}, \sigma_{zz}, \tau_{yz})^T$  from the fully 3D constitutive model is required at each fiber of the cross-section. To this end, classical approach is usually adopted [33], that is  $\epsilon_c$  is determined so that  $\sigma_c$  becomes zero. Because of the nonlinear material response, this commonly requires a nonlinear iterative process [32,34], involving the total stress and strain vectors and the incremental stress-strain relation in Eq. (14) linearized and properly partitioned. The components to be retained are denoted with subscript  $m$  and the components to be condensed with subscript  $c$ :

$$\sigma = \begin{Bmatrix} \sigma_m \\ \sigma_c \end{Bmatrix}, \quad \epsilon = \begin{Bmatrix} \epsilon_m \\ \epsilon_c \end{Bmatrix}, \quad \begin{Bmatrix} \Delta\sigma_m \\ \Delta\sigma_c \end{Bmatrix} = \begin{Bmatrix} \mathbf{C}_{mm} & \mathbf{C}_{mc} \\ \mathbf{C}_{cm} & \mathbf{C}_{cc} \end{Bmatrix} \begin{Bmatrix} \Delta\epsilon_m \\ \Delta\epsilon_c \end{Bmatrix} \quad (42)$$

Once the values of  $\epsilon_c$  components satisfying the condition  $\sigma_c = \mathbf{0}$  are evaluated, the condensed material tangent stiffness matrix is given by:

$$\mathbf{k}_m = \mathbf{C}_{mm} - \mathbf{C}_{mc}(\mathbf{C}_{cc})^{-1}\mathbf{C}_{cm} \quad (43)$$

where the subscript  $t$  is dropped to ease notation.

In this paper, a consistent non-iterative approach is proposed for the condensation process, taking advantage of the iterative solution scheme at the higher level of the element state determination: with the values of  $\epsilon_m^{l+1}$  and its increment  $\Delta\epsilon_m^{l+1}$  at the current element internal iteration  $l+1$ , the condensed strains  $\epsilon_c^l$  and the material stiffness matrix  $\mathbf{C}_t^l$  are recalled from the previous element iteration  $l$  and the steps in Table 5 are performed. Here, the increment of the condensed strains  $\epsilon_c$  are evaluated in step 1 and these are used in the material state of the full 3D model determination in step 2, that is in the determination of the stress vector  $\sigma$  and the material tangent stiffness matrix  $\mathbf{C}_t$ , for the given six strain quantities in  $\epsilon$ . Hence, the condensed strains are updated in step 3, considering the residual stresses  $\sigma_c$  that need to be zero, which are also used in step 4 to correct the retained stresses  $\sigma_m$ , according to the incremental constitutive relationship in Eq. (42). Finally, the material tangent stiffness matrix is evaluated in step 5 according to Eq. (43).

To be noted is that this approach assumes the behavior of the fibers as independent from each other, that is as if the area associated to the single fiber behaves independently from the adjacent ones. Hence, in-plane cross-section distortion and interaction between fibers is not accounted for. Similarly, transverse reinforcements are not explicitly included in the model. As shown in the numerical applications presented in Section 4, confinement effects due to transverse reinforcements are modeled by adequately increasing the strength and ductility of concrete fibers belonging to the confined regions of the cross-section. Further developments of the model are required to include in-plane distortion effects and have been left for future works.

A predictor-corrector solution procedure governs the full 3D material state determination of the plastic-damage model here used for concrete-like materials. First, in the elasto-plastic predictor phase the effective stresses  $\bar{\sigma}$  and elasto-plastic tangent stiffness  $\mathbf{C}^{ep}$  are computed. Then, in the damage corrector phase the damage variables  $D_t$  and  $D_c$ , the stress vector  $\sigma$  and the tangent stiffness matrix  $\mathbf{C}_t$  are evaluated.

In this paper, a consistent non-iterative approach is proposed for the condensation process, taking advantage of the iterative solution scheme at the higher level of the element state determination: with the values of  $\epsilon_m^{l+1}$  and its increment  $\Delta\epsilon_m^{l+1}$  at the current element internal iteration  $l+1$ , the condensed strains  $\epsilon_c^l$  and the material stiffness matrix  $\mathbf{C}_t^l$  are recalled from the previous element iteration  $l$  and the steps in Table 5 are performed. Here, the increment of the condensed strains  $\epsilon_c$  are evaluated in step 1 and these are used in the material state of the full 3D model determination in step 2, that is in the determination of the stress vector  $\sigma$  and the material tangent stiffness matrix  $\mathbf{C}_t$ , for the given six strain quantities in  $\epsilon$ . Hence, the condensed strains are updated in step 3, considering the residual stresses  $\sigma_c$  that need to be zero, which are also used in step 4 to correct the retained stresses  $\sigma_m$ , according to the incremental constitutive relationship in Eq. (42). Finally, the material tangent stiffness matrix is evaluated in step 5 according to Eq. (43). The procedure is summarized in Table 6, where the subscripts '  $n+1$  ' and '  $n$  ' denote the current and previous time steps,  $t_{n+1}$  and  $t_n$ , respectively.

Table 5. Non-iterative nonlinear static condensation of 3D material response.

1)	$\Delta\epsilon_c^{l+1} = -(\mathbf{C}_{cc}^l)^{-1}\mathbf{C}_{cc}^l\Delta\epsilon_m^{l+1} \rightarrow \epsilon_c^{l+1} = \epsilon_c^l + \Delta\epsilon_c^{l+1}$
2)	Material state determination in Table 6: $\epsilon^{l+1} \rightarrow \sigma^{l+1} = \sigma[\epsilon^{l+1}] \quad \text{and} \quad \mathbf{C}_t^{l+1} = \mathbf{C}_t[\epsilon^{l+1}]$
3)	$\Delta\epsilon_c^{l+1} = -(\mathbf{C}_{cc}^{l+1})^{-1}\sigma_c^{l+1} \rightarrow \epsilon_c^{l+1} = \epsilon_c^{l+1} + \Delta\epsilon_c^{l+1}$
4)	$\sigma_m^{l+1} = \sigma_m^{l+1} + \mathbf{C}_{mc}^{l+1}(\mathbf{C}_{cc}^{l+1})^{-1}\sigma_c^{l+1}$
5)	$\mathbf{k}_m^{l+1} = \mathbf{C}_{mm}^{l+1} - \mathbf{C}_{mc}^{l+1}(\mathbf{C}_{cc}^{l+1})^{-1}\mathbf{C}_{cm}^{l+1}$



Table 6. Material state determination

1)	State at $t_n$ set equal to the state at $l$ (Table 2)
	$\epsilon_{n+1} = \epsilon^{l+1}$ and $\Delta\epsilon_{n+1} = \epsilon^{l+1} - \epsilon^l$
Elasto-plastic predictor (damage evolution frozen at $t_n$ )	
2)	Elastic prediction
	$\epsilon_{n+1}^p = \epsilon_n^p$ , $\bar{\zeta}_{n+1} = \bar{\zeta}_n$ , $\alpha_{n+1} = \alpha_n$ and $\bar{\sigma}_{n+1} = \mathbf{C}(\epsilon_{n+1} - \epsilon_{n+1}^p)$
3)	If $f_{n+1} = f(\bar{\sigma}_{n+1}, \bar{\zeta}_{n+1}, \alpha_{n+1}) < 0 \rightarrow$ GO TO step 6)
	otherwise $\rightarrow$ GO TO step 4)
4)	Plastic correction
	$\lambda_{n+1} = \frac{f_{y,n+1}}{2G + 2/3(H_k + H_t)} \rightarrow \alpha_{n+1} = \alpha_n + \sqrt{\frac{2}{3}}\lambda_{n+1}$
	$\bar{\mathbf{n}}_{n+1} = \frac{\mathbf{P}\bar{\sigma}_{n+1} - \bar{\zeta}_n}{ \mathbf{P}\bar{\sigma}_{n+1} - \bar{\zeta}_n } \rightarrow \epsilon_{n+1}^p = \epsilon_n^p + \lambda_{n+1}\bar{\mathbf{n}}_{n+1}$
	$\bar{\zeta}_{n+1} = \frac{2}{3}H_k\epsilon_{n+1}^p$
5)	$\bar{\sigma}_{n+1} = \mathbf{C}(\epsilon_{n+1} - \epsilon_{n+1}^p)$ and $\mathbf{C}_{n+1}^{ep}$
Damage corrector (plastic strains frozen at $t_{n+1}$ )	
6)	Evaluate $\epsilon_{i,n+1}$ and $\epsilon_{i,n+1}^e$
7)	$e_{i,n+1}$ and $e_{i,n+1}^e$ from Eq. (21)
	$Y_{h,n+1}$ and $Y_{h,n+1}^e$ from Eq. (20) for $h = t, c$
8)	$f_{h,n+1} = Y_{h,n+1} - Y_{0h} - (a_h Y_{h,n+1} + k_h)D_{h,n}$
	If $f_{h,n+1} < 0 \rightarrow D_{h,n+1} = D_{h,n}$ ,
	otherwise $\rightarrow D_{h,n+1} = \frac{Y_{h,n+1} - Y_{0h}}{a_h Y_{h,n+1} + k_h}$ with $D_h \in [D_{h,n}, 1]$ for $h = t, c$
9)	$\eta_{h,n+1} = \frac{Y_{h,n+1}^e}{Y_{0h,n+1} + (a_{h,n+1} Y_{h,n+1}^e + k_{h,n+1})D_n}$
10)	$\alpha_{t,n+1} = \frac{\eta_{t,n+1}^2}{\eta_{t,n+1}^2 + \eta_{c,n+1}^2}$ and $\alpha_{c,n+1} = 1 - \alpha_{t,n+1}$
11)	$D_{n+1} = \alpha_{t,n+1}D_{t,n+1} + \alpha_{c,n+1}D_{c,n+1}$
12)	$\sigma_{n+1} = (1 - D_{n+1})^2 \mathbf{C}(\epsilon_{n+1} - \epsilon_{n+1}^p)$ and $\mathbf{C}_{t,n+1} = (1 - D_{n+1})^2 \mathbf{C}_{n+1}^{ep}$

In the last step of the damage corrector phase, the matrix  $\mathbf{C}_t$  is evaluated by neglecting the term depending on  $\partial D / \partial \epsilon$  in Eq. (14) [48], that is by adopting a secant formulation for the damage evolution process. When considering softening material behaviors, this usually leads to higher stability of the solution algorithms. However, this reduces the convergence rate and, thus, requires higher computational burden. This issue is particularly important for the condensation procedure described above. As the total stresses in Eq. (13) are defined as the product of the effective stresses  $\bar{\sigma}$  and the scalar quantity  $(1 - D)^2$ , to increase convergence speed, the condensation procedure can be directly applied to the effective stresses, when the elasto-plastic predictor phase is completed. Hence, the values of  $\epsilon_c$  that satisfy the condition  $\bar{\sigma}_c = \mathbf{0}$  are found, before starting the damage correction phase. This is accomplished by exploiting same equations as those in Table 5, yet written in terms of effective stresses  $\bar{\sigma}$  and elasto-plastic tangent stiffness  $\mathbf{C}^{ep}$ . Thus, quadratic convergence of the condensation procedure is guaranteed without loss of numerical stability.

### 4. Numerical Simulations

This section presents three numerical applications performed to validate the efficiency and accuracy of the presented beam FE formulation. The first considers a U-shaped RC wall subjected to bi-axial cyclic horizontal loads and exhibiting prominent shear deformations. The second refers to a series of RC prismatic beams, subjected to monotonic end torsional loads, where cross-section warping plays a primary role in the damaging process of the specimens. The third simulates the behavior of a steel L frame under cyclic torsional load, where transmission of warping occurs between the column and the beam at the connection joint.



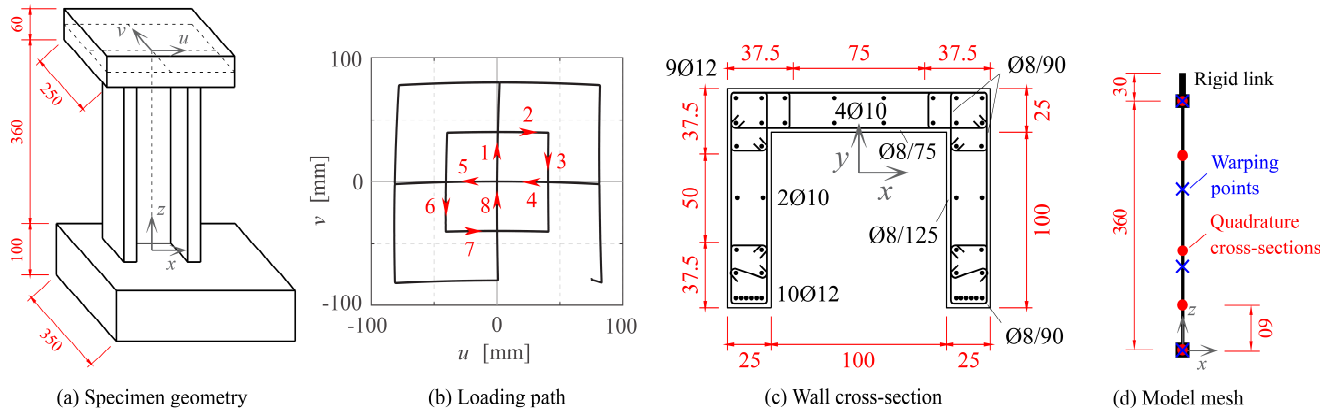


Fig. 4. U-shaped RC shear wall: (a) geometry, (b) loading path, (c) cross-section (dimensions in cm) and (d) mesh details

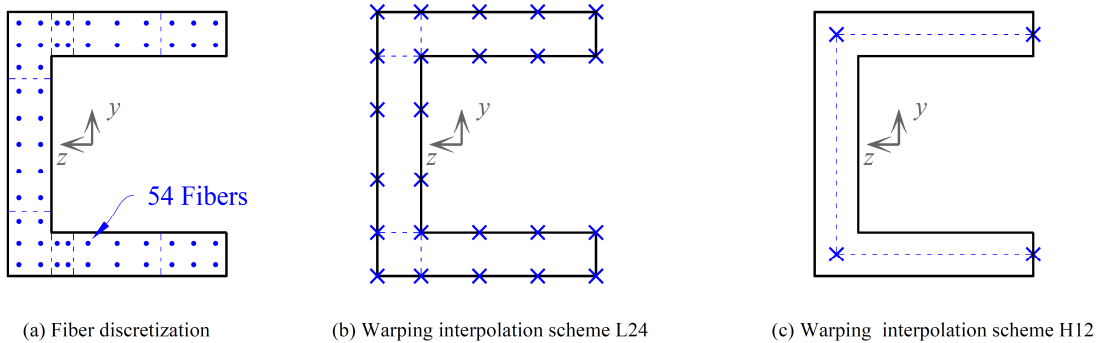


Fig. 5. U-shaped RC shear wall: (a) fiber discretization for evaluating the material response and warping displacement interpolation scheme with (b) Lagrange and (c) Hermite polynomials

4.1 RC U-shaped wall under bi-axial cyclic lateral forces

The first numerical application reproduces the experimental test by Pegon et al. [49] on the RC U-shaped shear wall in Fig. 4. The focus is on the performance of the adopted FE model in representing the effects of the warping and its coupling with the damaging phenomena when cyclic transverse loads are applied to the beam elements.

The wall is horizontally loaded at the top in both  $x$  and  $y$  directions, controlling the displacements  $u$  and  $v$  according to the butterfly path in Fig. 4b. Four butterfly cycles with two different amplitudes characterize the loading path. The red arrows in the figure indicate the shape of the first cycle, where the maximum displacement in both the directions is almost 40 mm; the second cycle is symmetric to the first one with respect to the  $v$ -axis, that is it involves the negative-positive and the positive-negative combinations of the displacements; finally, the third and fourth cycles have the same shape of the first two, but they reach a maximum displacement of 80 mm. The forces act in the mid-plane of the top slab, i.e., the shear span ratio is equal to  $L = 3.90m$ ; the constant axial compression is equal to 2000 kN.

One FE models the whole deformable part of the wall, assuming the top and the bottom square slabs as rigid and the warping displacements restrained at both the end sections [50]. Details of the adopted mesh are depicted in Fig. 4d. Four equally spaced warping points,  $n_w = 4$ , and five quadrature cross-sections are placed over the height. Weighting length associated to the base quadrature cross-section, where stresses reach their maximum values, is set equal to  $L/6$ , to regularize the element response [47], while the remaining four cross-sections are distributed according to the Gauss-Lobatto quadrature rule in the upper portion of the element having length 300 cm, i.e. quadrature cross-section positions are  $x = 0$  cm, 60 cm, 127.08 cm, 194.16 cm and 360 cm.

Fig. 5a shows the fiber discretization of the cross-section and Fig. 5b and Fig. 5c show two interpolation schemes for the warping points. Both schemes consider a cubic variation of the warping displacement along web and flanges, and a linear variation across the thickness. However, the L24 scheme, adopting Lagrange polynomials, uses 24 warping DOFs, whereas the H12 scheme, adopting Hermite polynomials, uses only 12 warping DOFs.

Table 7 lists the material parameters for the unconfined concrete. The strength increase in the confined parts, that is at tips of the flanges and at the intersections between these and the web, is reproduced by setting  $k_c = 2.8 \cdot 10^{-3}$  and  $a_c = 0.8$ . The Giuffrè-Menegotto-Pinto model [39] describes the behavior of the steel reinforcing bars, with  $E^s = 200000MPa$ ,  $\sigma_y^s = 540MPa$  and  $b = 1.0\%$  being the Young's modulus, plastic yield strength and ratio between hardening and elastic stiffness, respectively. The transition coefficient  $R$  from elastic to plastic state needed in the model result from the following parameters:  $R_0 = 20$ ,  $a_1 = 18.5$  and  $a_2 = 0.15$  and no isotropic hardening is assumed.

Table 7. Material parameters for the cyclic uni-axial material response in Fig. 3.

$E$	$\nu$	$\sigma_t$	$\sigma_c$	$H_k$	$H_l$	$Y_{ot}$	$k_t$	$a_t$	$Y_{oc}$	$k_c$	$a_c$	$\beta$
28GPa	0.25	3.3MPa	30MPa	0.8E	0.001E	$6.7 \cdot 10^{-5}$	$2.0 \cdot 10^{-5}$	0.8	$4.0 \cdot 10^{-4}$	$2.0 \cdot 10^{-3}$	0.4	0.5



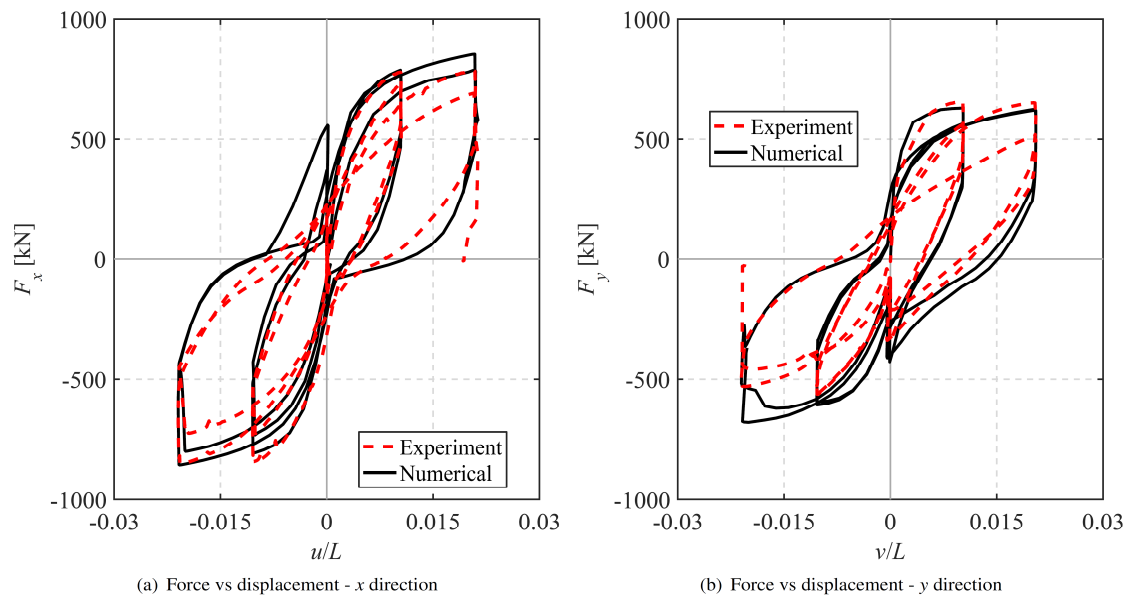


Fig. 6. U-shaped RC shear wall: global response in terms of applied horizontal loads  $F_x$  and  $F_y$  vs top displacements  $u$  and  $v$

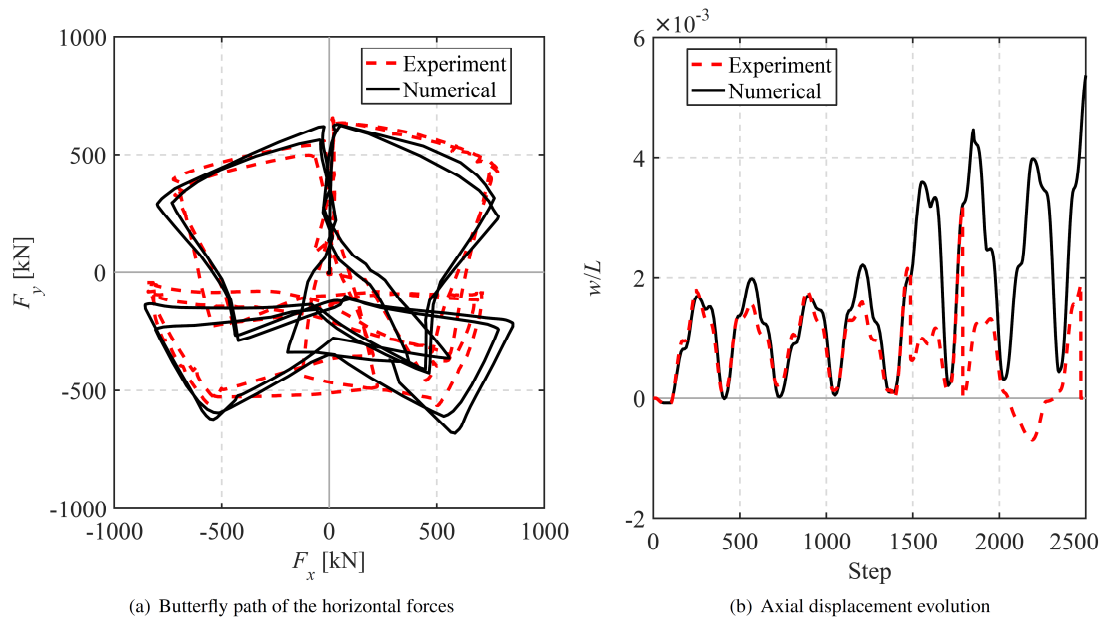


Fig. 7. U-shaped RC shear wall: global response in terms of applied loads  $F_x$  vs  $F_y$  and normalized top vertical displacement  $w/L$

As the global solutions for the two warping interpolation schemes L24 and H12 coincide, since the order of the warping interpolation over the cross-section is the same, Fig. 6 plots only the results for the H12 scheme, showing the evolution of the applied horizontal loads  $F_x$  and  $F_y$  in the two directions vs the normalized top displacements  $u/L$  and  $v/L$ . Similarly, Fig. 7a shows the relation between these forces and Fig. 7b the evolution of the normalized top vertical displacement  $w/L$  during the loading history. The numerical results (black solid curves) show the good ability of the model in describing the strength loss occurring for subsequent cycles. A certain gap between numerical and experimental (red dashed curves) solutions occurs only in the last cycles, in particular for the response in the  $y$  direction. Indeed, the strength loss observed in the real specimen is caused by the reinforcing bar failure, which leads to the structural collapse in the last cycle. By contrast, the numerical constitutive relationship representing the behavior of the steel reinforcing bars does not include the material degradation and, thus, cannot capture this failure mechanism.

Finally, Fig. 8 compares the total vertical displacements  $u(x,y,z)$  at (a) the mid-height cross-section ( $z = 1.8\text{m}$ ) and (b) the top cross-section ( $z = 3.6\text{m}$ ) at the end of the first loading in the  $x$  direction, that is loading phase 2 in Fig. 4b. For the mid-height cross-section, the solution of the adopted beam model, considering the interpolation scheme H12 and that obtained with a 4-node MITC shell FE model [51] are compared. It is evident that the adopted beam model can reproduce the cross-section warping deformation, here representing an important contribution of the total axial material displacement  $u$ . For the top cross-section, the comparison also involves the experimental outcomes from [49]. The results show that the adopted beam model correctly accounts for the warping constraints and reproduces the plane-section displacements induced by the top slab.



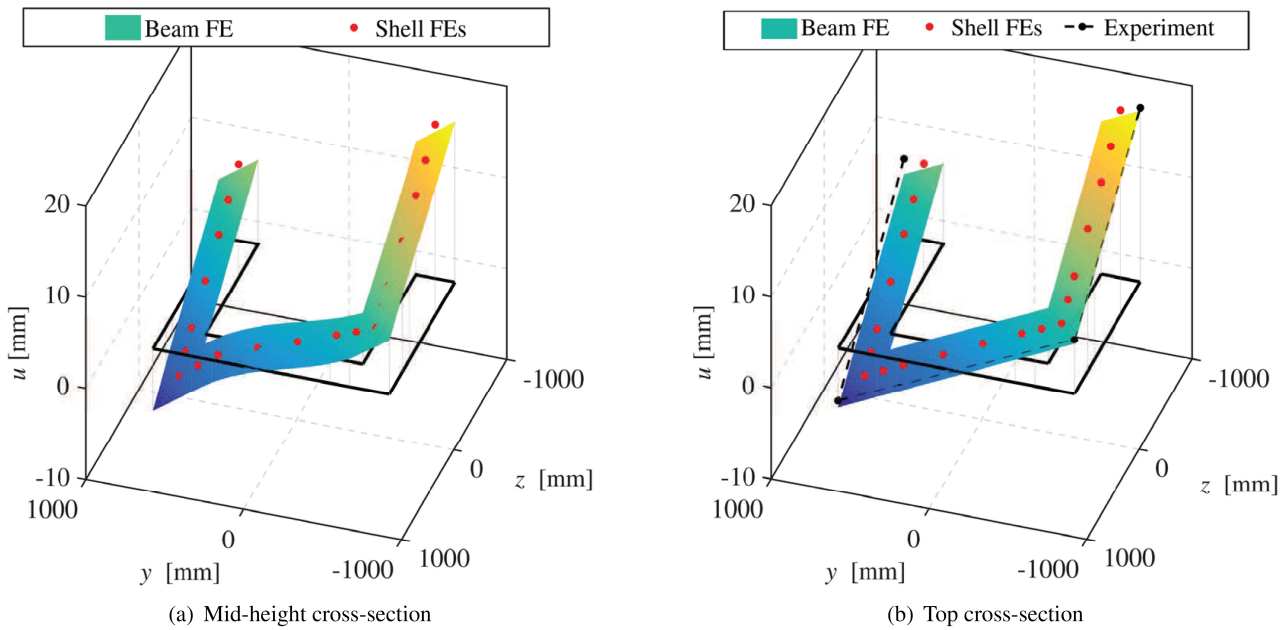


Fig. 8. Total vertical displacements  $u$  at the mid-height and top sections in the RC U-shaped shear wall

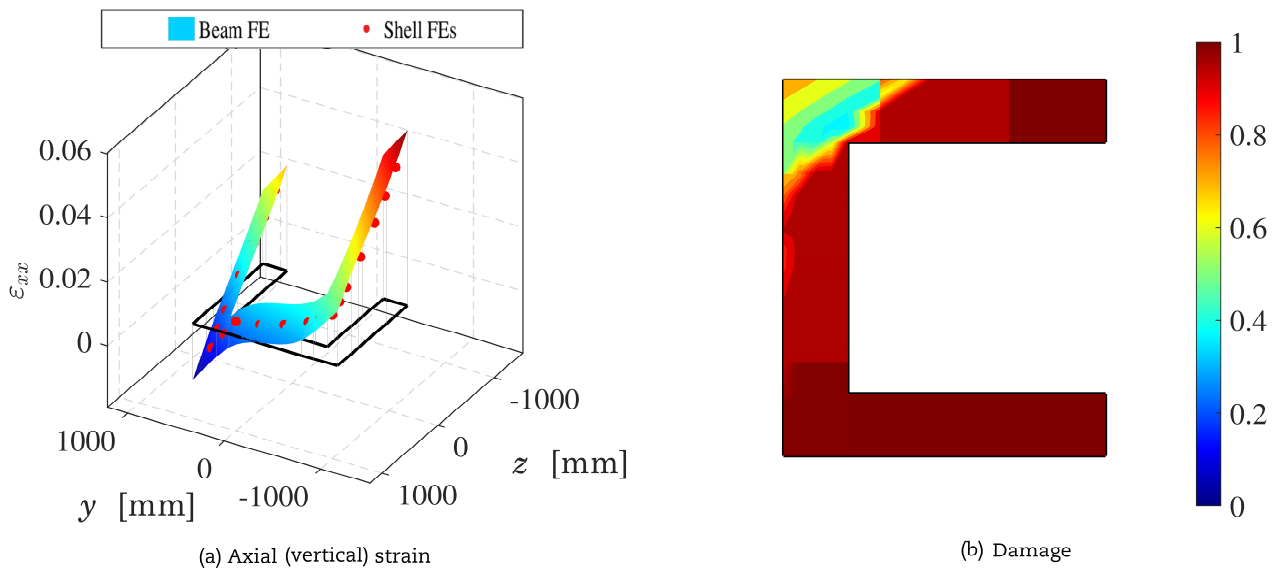


Fig. 9. Response of the base cross-section ( $x = 0$ ) of the RC U-shaped shear wall

Results for the base of the wall are not reported as both plane-section and warping displacements are null at this cross-section. However, to analyze the interaction between warping and shear-lag effects, Fig. 9a plots the variation of the axial (vertical) strain obtained at  $x = 0$  with the beam FE model (colored surface). This is compared with that resulting from the shell model (red dots). As shown, strain profile differs from that occurring under rigid plane cross-section assumption and is characterized by evident undulation due to warping. This also influences the variation of damage distribution over the cross section, that is depicted in Fig. 9b as contour plot. For this quantity, interaction with warping deformation is less evident, as most part of the cross-section undergoes severe damage due to tension (red area). Only a small area (green-yellow corner) is under compression and results as partially damaged. Further discussion on the performances of the proposed model in reproducing boundary condition effects in terms of strain and stress variation is reported in previous works [20, 21].

#### 4.2 RC prismatic beams under torsional loads

The second numerical application concerns the experimental tests performed by Chalioris [52] for three RC beams under torsional loads. All the specimens have a total length of 160cm and are divided into three parts: two end parts of length  $L_e$ , reinforced so as to exhibit an elastic response, and a middle part of length  $L$  undergoing cracking and damage (Fig. 10a). At both the ends a monotonically increasing torsional couple  $M_x$  is applied. Only the damaging middle part is modeled in the numerical analysis, using one beam FE with three Gauss-Lobatto quadrature cross-sections.



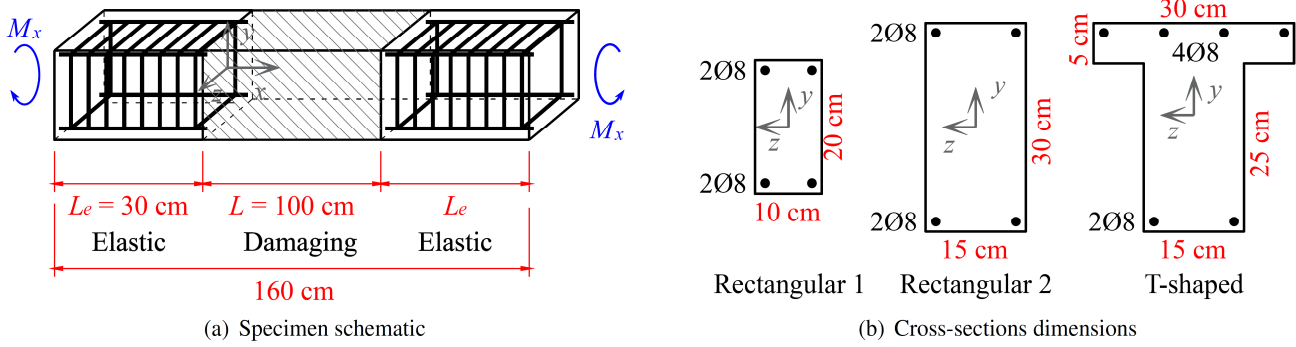


Fig. 10. Geometry of the prismatic beams subjected to torsional loads

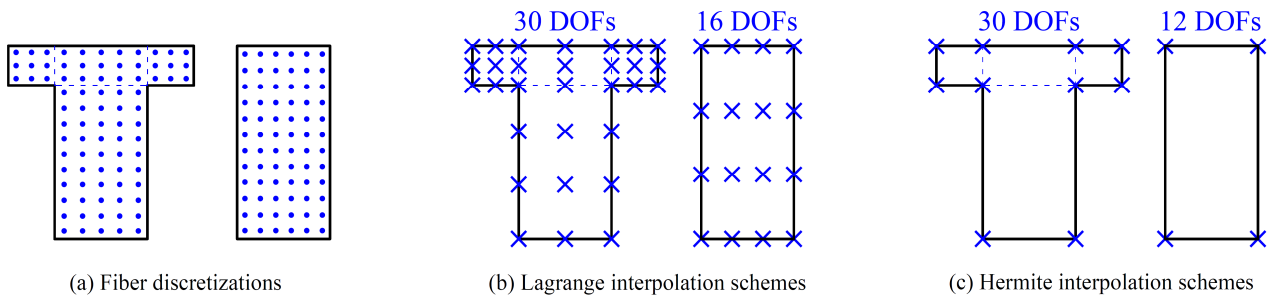


Fig. 11. RC beams under torsional load: (a) cross-section fiber discretization and warping displacement interpolation schemes adopting (b) Lagrange and (c) Hermite polynomials

The three cross-section shapes in Fig. 10b are considered, with a midpoint fiber discretization that uses 72 fibers for the rectangular cross-sections and 83 fibers for the T-shaped one (Fig. 11a). The reinforcing bars are treated as additional fibers.

The cross-section warping displacements are assumed to be free, producing uniform warping along the entire element length. Hence,  $n_w = 1$  is assumed.

Table 8 contains the value of the material parameters adopted for each specimen, with  $\nu = 0.2$ ,  $\sigma_c = 30\text{MPa}$ ,  $H_i = 0.001E$ ,  $H_k = 0.7E$ ,  $Y_{0c} = 5Y_{0t}$ ,  $k_c = 5.0 \cdot 10^{-3}$ ,  $\alpha_c = 0.2$  and  $\beta = 1.0$  for all of them. The classical J2 plasticity model [31] is adopted for the steel reinforcing bars, being  $E^s = 210000\text{MPa}$  the Young's modulus,  $\nu^s = 0.3$  the Poisson coefficient,  $\sigma_y^s = 560\text{MPa}$  the uni-axial yielding stress and  $H_i^s = 0.001E$  and  $H_k^s = 0.01E$  the isotropic and kinematic hardening moduli, respectively.

Each beam considers two different interpolation schemes for the warping DOFs over the cross-sections, as depicted in Fig. 11b and Fig. 11c, assuming either Lagrange or Hermite interpolation polynomials. All schemes provide cubic interpolation of the warping displacements  $u_w$  in both  $y$  and  $z$  directions, except for the Lagrange scheme of the T-shaped section, where the interpolation order is quadratic.

Fig. 12 compares the numerical response of the three beams with the experimental data (red dotted curves), in terms of applied couple  $M_x$  vs average rate of the angle of twist  $\theta_x / L$ . The results for both the Lagrange (green dashed curves) and Hermite (black solid curves with crosses) interpolation schemes coincide for the rectangular beams, as the two interpolations have the same order, and slightly differ for the T-shaped one, as the order of interpolation is comparable but not coinciding. In all cases, the numerical response satisfactorily reproduces the experimental results, well detecting the initial stiffness, the pick strength, and the degrading mechanism of the beams. The experiments show greater strength for the post-peak branch of curves, as the beams approach their final collapsing state, but this behavior due to rough cracks, dowel action and nonlinear geometric transverse deformations of the bars is not accounted for in the adopted numerical model.

Fig. 12 also compares the numerical results with those obtained with a standard Timoshenko beam FE (blue dashed curves), that is under the assumption of rigid cross-section, correcting the torsional inertia  $J$  through the semi-analytical solutions based on the Fourier series to account for warping.  $J$  results equal to  $6774\text{cm}^4$  for the T-shaped and equal to  $\alpha hb^3$  for the rectangular shape,  $h$  and  $b$  being the cross-section depth and width;  $\alpha = 0.2291$  for Rectangular 1 and  $\alpha = 0.2635$  for Rectangular 2. The figure shows that the rigid section assumption highly overestimates the beam strength, since this does not correctly capture the material state evolution during the loading path [20,48]. The resulting shear/strain distribution over the cross-section is similar to that of a circular beam, regardless of the real shape of the cross-section. Fig. 13 compares the distribution of (a) the damage variable  $D$  and (b) the maximum principal in-plane stress, which is due to shear, for the standard T-shaped FE and the corresponding enhanced model with the Hermite interpolation scheme. The gray dashes in Fig. 13b indicate the direction of the plotted principal stress. As shown, the adopted enhanced model gives correct information on the actual trend of damage and stress distributions, which depends on the warping displacements  $u_w$  (Fig. 14). Completely different solutions are obtained with the standard beam model.





**Table 8.** Material parameters for concrete model in prismatic beams under torsional loads.

	$E$	$\sigma_t$	$Y_{0t}$	$k_t$	$a_t$
Rectangular 1	20 GPa	12 MPa	$9.72 \cdot 10^{-5}$	$2.4 \cdot 10^{-4}$	0.8
Rectangular 2	20 GPa	12 MPa	$5.40 \cdot 10^{-5}$	$2.5 \cdot 10^{-4}$	1.0
T-shaped	30 GPa	21 MPa	$7.20 \cdot 10^{-5}$	$1.0 \cdot 10^{-4}$	1.0

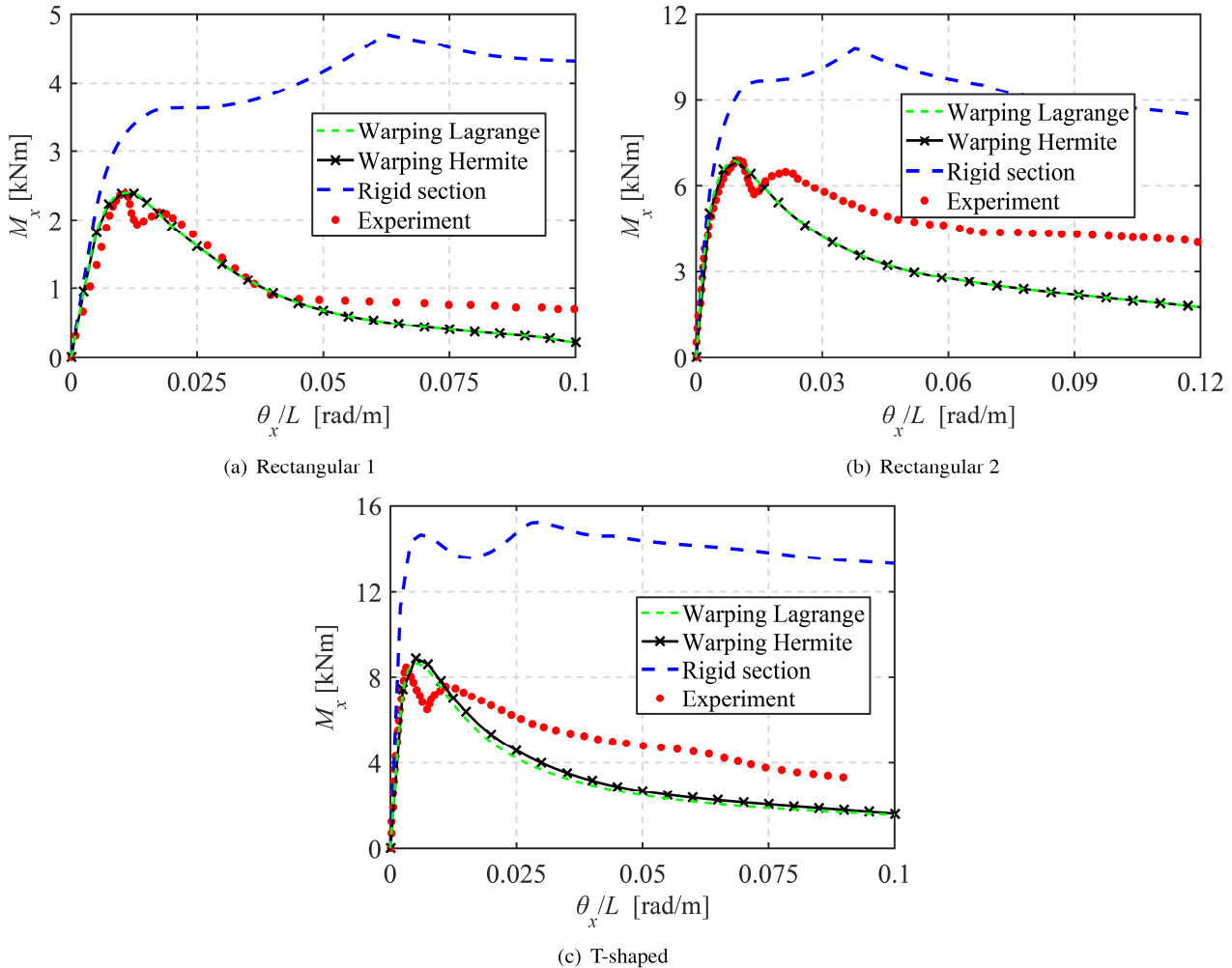


**Fig. 12.** Response of the RC beams subjected to end torsional loads: moment vs rotation per unit length

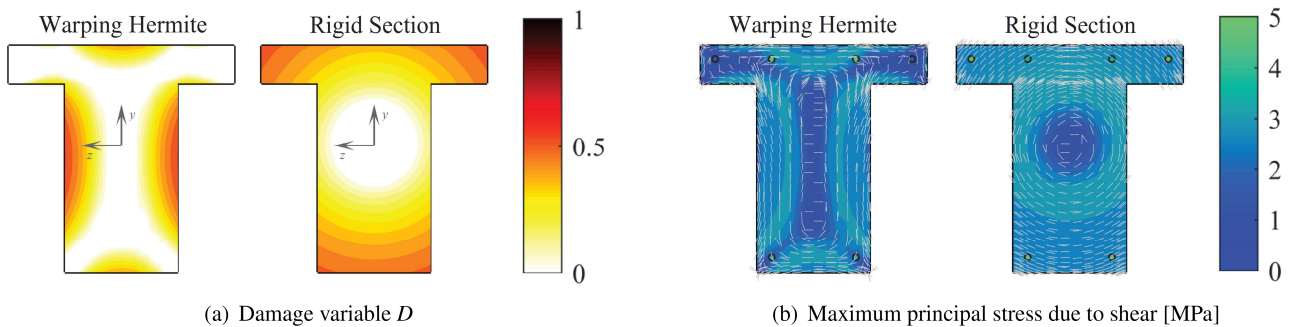


**Fig. 13.** Distribution of damage and maximum principal stress over the T-shaped cross-section with and without warping, at  $\theta_x / L = 0.006 \text{ rad/m}$

To investigate the performances of the solution algorithm proposed for the element state determination, the numerical analyses of the beams are performed by adopting both the iterative procedure, as described in Table 2, and the non-iterative procedure that results by setting the maximum number of internal iterations in Table 3 to one. Identical responses are obtained for the two cases and Table 9 reports the computational time required for each analysis, evaluated as the average value of ten simulation per each test, and the total number of global N-R and internal element iterations. The total number of load steps assumed for the analyses is also given. Only the Lagrange interpolation scheme is considered for this comparison.



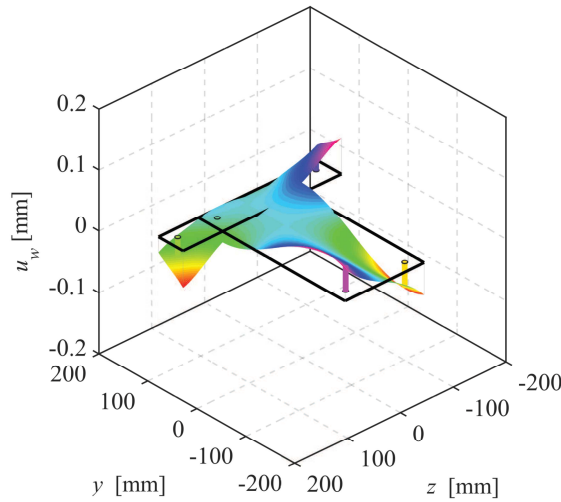


Fig. 14. Warping displacement in the T-shaped RC beam subjected to end torsional loads, at  $\theta_x / L = 0.006\text{rad/m}$

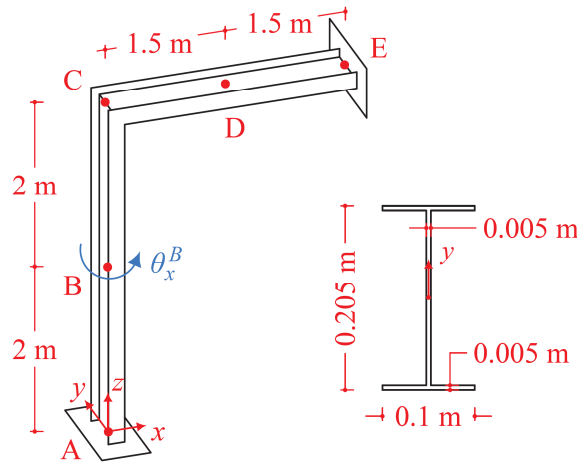


Fig. 15. Geometry of the steel L frame with flange continuity

As expected, computational time is strongly determined by the total number of internal element iterations, having fixed all other model data, e.g. number of load steps, residual tolerance, number of FEs, number of DOFs, number of fibers, etc.. For the rectangular beams, the non-iterative algorithm results significantly more efficient than the iterative one, as the total number of internal iterations is lower in this case. However, similar computational burden is required by the two solution schemes for the T-shaped beam. In this case, when the non-iterative solution algorithm is adopted, at each N-R iteration higher residual internal forces are passed by the element to the global solution program and more attempts are needed to reach convergence than those required when the iterative algorithm is used.

**4.3 Steel L frame with flange continuity**

The third test analyzes the behavior of the steel frame depicted in Fig. 15. This is composed by I-shaped column and beam having same cross-section geometry and length equal to 4 m and 3 m, respectively.

Table 9. RC beams subjected to end torsional loads: required total global N-R iterations and total internal iterations for the non-iterative and iterative element state determination scheme.

	Algorithm	N-R iterations	Internal iterations	Total load steps
Rectangular 1	Non-iterative	91.3 s	211	100
	Iterative	479.8 s	835	100
Rectangular 2	Non-iterative	80.3 s	215	100
	Iterative	276.8 s	495	100
T-shaped	Non-iterative	516.7 s	985	200
	Iterative	511.4 s	979	200



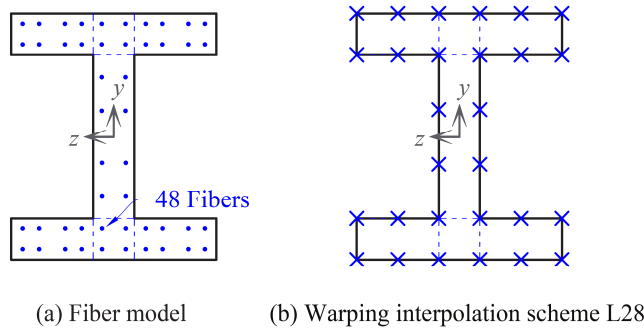


Fig. 16. Steel L frame with flange continuity: (a) fiber discretization for material response and (b) warping displacement interpolation scheme

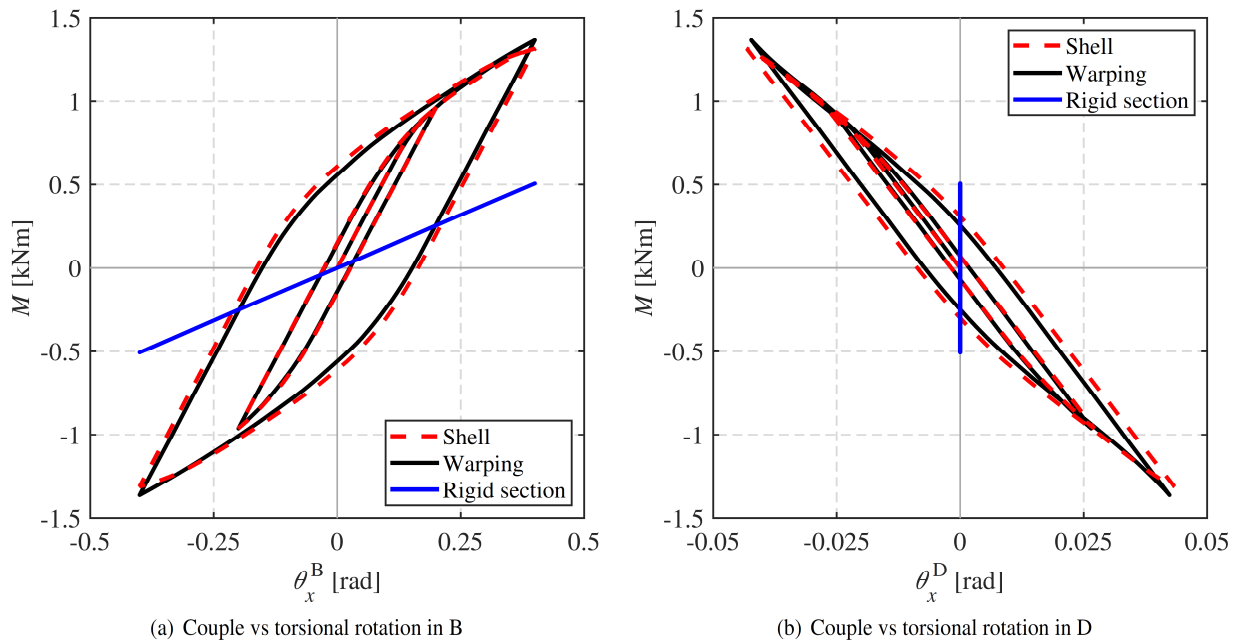


Fig. 17. Steel L frame with flange continuity: global response in terms of resisting couple  $M$  vs torsional rotations  $\theta_x^B$  (applied) and  $\theta_x^D$  of cross-sections B and D, respectively

Cross-section orientation is such that flange continuity is obtained at the beam-column connection joint (point C in the figure). Plane-section and warping displacements are prevented at the ends of the frame (points A and E), as well as the transverse displacement along  $y$  direction of point C. The frame is loaded by controlling the torsional rotation,  $\theta_x^B$ , of the cross-section in B. This varies by following a cyclic pattern that considers the following limit values:

$$\theta_x^B = 0\text{rad} \rightarrow 0.2\text{rad} \rightarrow -0.2\text{rad} \rightarrow 0.4\text{rad} \rightarrow -0.4\text{rad} \rightarrow 0.4\text{rad}$$

Elasto-plastic material response is assumed. Thus, J2 plasticity model with linear kinematic hardening is adopted, with Young's modulus  $E^s = 205000\text{MPa}$ , Poisson ratio  $\nu^s = 0.3$ , yielding stress  $\sigma_y^s = 150\text{MPa}$  and hardening modulus  $H_k^s = 0.01E^s$ .

The frame is modeled by adopting a uniform mesh made of six and eight proposed FEs for beam and column, respectively, with cubic warping interpolation assumed along the element axis, i.e.,  $n_w = 4$ . All FEs consider the additional warping DOFs placed at the end nodes as external variables, so that warping continuity is ensured both along the members and at the joint. Indeed, due to the particular orientation, the end cross-sections of beam and column that meet at the joint C undergo equal warping profile. Hence, when column twists, warping of the top cross-section produces warping in the beam, which is expected to twist as well. This is shown in [53-55], where similar specimen is analyzed under monotonic loads and assuming linear elastic material response. Different orientations of the element cross-sections are considered there, so that warping transmission at the joint is influenced by the configuration of the stiffeners eventually placed to prevent joint distortions.

Fig. 16a shows the fiber discretization adopted for the cross-section, whose thickness is enlarged in the picture for better representation. In this case, fibers are distributed according to the Gauss-Legendre rule, as exact integration of the element torsional stiffness is required to obtain the correct response of the frame. Fig. 16b shows the interpolation scheme for the warping points. This adopts Lagrange polynomials and assumes parabolic and cubic warping interpolation along web and flanges, respectively, and linear interpolation across the membrature thickness. The total number of warping DOFs over each cross-section is  $m_w = 28$ .



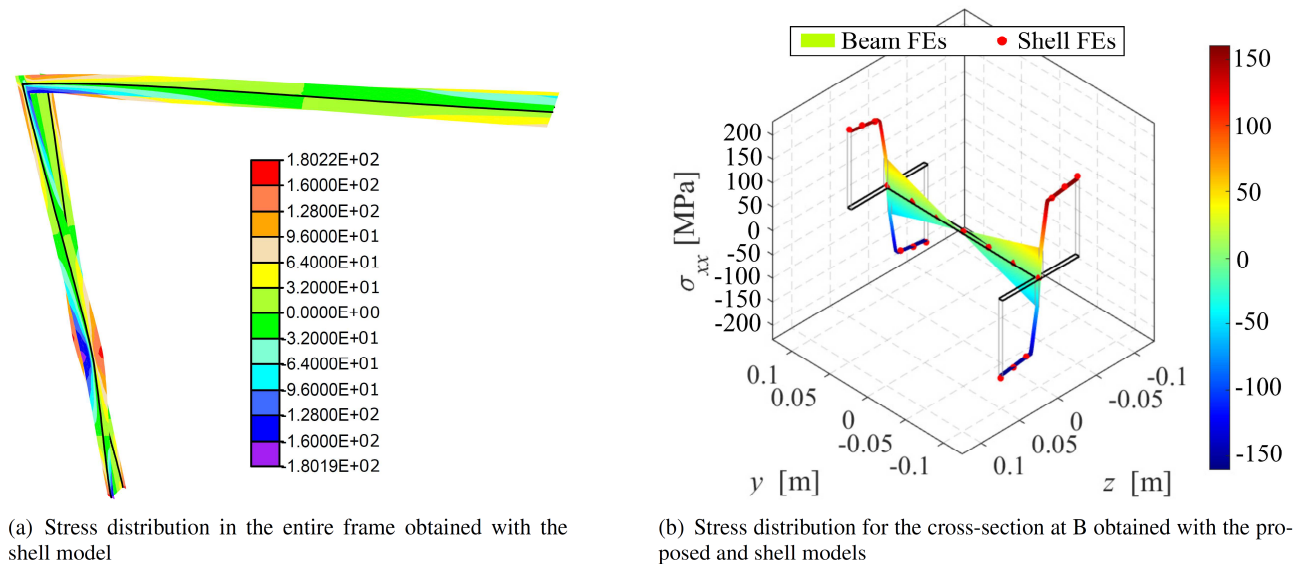


Fig. 18. Axial stresses  $\sigma_{xx}$  [MPa] in the L frame with flange continuity for  $\theta_x^B = 0.04$  rad

Fig. 17 shows the solution obtained in terms of total torsional resisting couple  $M$ , acting about the vertical direction at the restraints and corresponding to the couple required in B to impose the desired rotation  $\theta_x^B$ . This is plotted against the torsional rotation  $\theta_x$  of (a) the mid-height cross-section of the column and (b) the mid-span cross-section of the beam, referred to the element local axes  $x$ . Dashed red curves represent the reference solutions obtained with a shell model. This is defined in FEAP [56] considering a mesh of 2268 4-node Discrete Kirchhoff Quadrilateral (DKQ) elements. Solid black curves refer to the results obtained with the proposed model and solid blue curves indicate those obtained with a standard beam assuming rigid cross-section. For this latter, cross-section torsional inertia is computed according to the thin-walled beam theory and results equal to  $J = \kappa_t I_p$ , being  $I_p$  the cross-section polar inertia and  $\kappa_t = 0.001153$  the correction coefficient.

Proposed FE perfectly agrees with the shell model and captures the warping transmission at the joint, showing the torsional rotation occurring in the beam (Fig. 17b) and the correct material plastic evolution. Due to warping constraints, torsion of the members induces significant shear-lag effects and the related axial stresses produce yielding of the material at cross-sections A, B and C (for both members). By contrast, standard beam model does not consider boundary warping restraints and, thus, provides a significantly more flexible response. In addition, this does not capture shear-lag and always provides a linear elastic solution.

Distribution of the axial stress  $\sigma_{xx}$  is plotted in Fig. 18 when  $\theta_x^B$  reaches for the first time the value 0.04 rad. Fig. 18a shows the variation obtained with the shell model in the entire frame. Stresses are plotted for the visible face of the shell FEs. While, Fig. 18b shows the variation occurring over the cross-section in B and compares the results obtained with the beam model with warping (colored surface) with those obtained with the shell model (red dots). For this latter, projected node values are plotted, i.e. values of the stresses evaluated at the nodes of the FE mesh. These perfectly agree with those attained at the mid-line of the beam cross-section.

Although limited to linear elastic case, similar analyses are presented in [55] for a specimen with similar geometry but different orientation of element cross-section, showing the variation along the beam and column axis of the axial stress,  $\sigma_{xx}$ , obtained with the proposed model and compared with a shell FE solution. These phenomena related to shear-lag effect have been widely studied in previous works [20, 21, 55] and are beyond the scope of this paper, which mainly focuses on the computational enhancements introduced for the proposed formulation. Hence, they are not discussed here.

## 5. Conclusion

This paper focused on the computational enhancements concerning the enhanced 3D beam FE model presented by Di Re et al. [21] for the analysis of RC structural beams subjected to relevant shear and torsional loads and including cross-section warping. All the computational details for its implementation in general FE analysis codes were described. Constitutive models with plasticity and damage were adopted to simulate steel and RC structural elements nonlinear response. In particular, a 3D plastic-damage material model was introduced for concrete in the framework of the fiber discretization procedure to investigate the influence of non-uniform shear stress-strain distributions and their interaction with the damaging process.

The paper presented an enhanced solution algorithm, with respect to that proposed by Le Corvec [19]. This permitted to adopt the model for the analysis of damaging structures that exhibit softening material behavior and, if required, to by-pass the iterative procedure used to enforce simultaneously the element equilibrium and compatibility conditions, as usual for force-based and mixed beam FEs. Moreover, the study proposed a new efficient technique to condense out the in-plane stress components, involved in the 3D constitutive model description but not directly included in the fiber section formulation. The proposed procedure considers a non-iterative scheme that takes advantage of the global iterative solution scheme and avoids the inner loop.

Three numerical applications were conducted to validate the presented numerical model: the analysis of a RC U-shaped shear wall under lateral forces, that of three RC prismatic beams under torsional loads and that of a steel L frame with flange continuity



under cyclic torsional load. All the solution algorithms adopted for the FE models were proved to be computationally efficient and accurate, even under complex loading conditions. Both the non-iterative element state determination and condensation procedures resulted less time consuming than the classical iterative ones and did not introduce any complication in the model implementation.

Moreover, numerical analysis discussed the importance of modeling warping effects and warping boundary restraints, when relevant torsional actions are present, focusing on the interaction between out-of-plane cross-section deformations and plastic and damage phenomena. As expected, classical beam models, based on the rigid cross-section assumption, give incorrect results, since cross-section deformation and shear-lag effects are not correctly reproduced, and fail in representing the real evolution of plasticity and damaging effects in the material. By contrast, the adopted enhanced model correctly reproduces the cross-section deformation displacements and their variation along the element axis and, thus, captures the actual stress-strain distribution and the evolution of plastic strains and damage quantities due to out-of-plane warping.

### Author Contributions

All authors planned the scheme, initiated the project, developed the mathematical modeling, examined the theory validation and conducted the numerical tests. The manuscript was written through the contribution of all authors. All authors discussed the results, reviewed, and approved the final version of the manuscript.

### Acknowledgments

Authors acknowledge the grant PRIN-2017 20173C478N.

### Conflict of Interest

The authors declared no potential conflicts of interest with respect to the research, authorship, and publication of this article.

### Funding

The authors received no financial support for the research, authorship, and publication of this article.

### Data Availability Statements

The datasets generated and/or analyzed during the current study are available from the corresponding author on reasonable request.

### References


- [1] Rabczuk, T., Zi, G., Bordas, S., Nguyen-Xuan, H., A geometrically non-linear three-dimensional cohesive crack method for reinforced concrete structures. *Engineering Fracture Mechanics*, 75(16), 2008, 4740-4758.
- [2] Areias, P., Rabczuk, T., Finite strain fracture of plates and shells with configurational forces and edge rotations. *International Journal for Numerical Methods in Engineering*, 94(12), 2013, 1099-1122.
- [3] Ciampi, V., Carlesimo, L., A nonlinear beam element for seismic analysis of structures. *8th European Conference on Earthquake Engineering*, 1986.
- [4] Ayoub, A., Filippou, F. C., Mixed formulation of nonlinear steel-concrete composite beam element. *Journal of Structural Engineering-ASCE*, 126(3), 2000, 371-381.
- [5] Taylor, R. L., Filippou, F. C., Saritas, A., Auricchio, F., A mixed finite element method for beam and frame problems. *Computational Mechanics*, 31(1), 2003, 192-203.
- [6] Alemdar, B. N., White, D. W., Displacement, flexibility, and mixed beam-column finite element formulations for distributed plasticity analysis. *Journal of Structural Engineering-ASCE*, 131(12), 2005, 1811-1819.
- [7] Bairán García, J.M., A non-linear coupled model for the analysis of reinforced concrete sections under bending, shear, torsion and axial forces. Ph.D. Thesis, Universitat Politècnica de Catalunya, 2005.
- [8] Ceresa, P., Petrini, L., Pinho, R., Flexure-shear fiber beam-column elements for modeling frame structures under seismic loading - State of the art. *Journal of Earthquake Engineering*, 11(S1), 2007, 46-88.
- [9] Bairan, J.M., Mari, A.R., Multiaxial-coupled analysis of RC cross-sections subjected to combined forces. *Engineering Structures*, 29(8), 2007, 1722-1738.
- [10] Mohr, S., Bairán, J.M., Mari, A.R., A frame element model for the analysis of reinforced concrete structures under shear and bending. *Engineering Structures*, 32(12), 2010, 3936-3954.
- [11] Poliotti, M., Bairán, J.M., B-spline sectional model for general 3D effects in reinforced concrete elements. *Engineering Structures*, 207, 2020, 110200.
- [12] Kagermanov, A., Ceresa, P., 3D fiber-based frame element with multiaxial stress interaction for RC structures. *Advances in Civil Engineering*, 2018, 1-13.
- [13] Saritas, A., Filippou, F.C., Inelastic axial-flexure-shear coupling in a mixed formulation beam finite element. *International Journal of Non-Linear Mechanics*, 44(8), 2009, 913-922.
- [14] Ferradi, M.K., Cespedes, X., A new beam element with transversal and warping eigenmodes. *Computers & Structures*, 131, 2014, 12-33.
- [15] Vieira, R.F., Virtuoso, F.B.E., Pereira, E.B.R., A higher order thin-walled beam model including warping and shear modes. *International Journal of Mechanical Sciences*, 66, 2013, 67-82.
- [16] Dikaros, I.C., Sapountzakis, E.J., Generalized warping analysis of composite beams of an arbitrary cross section by BEM. I: Theoretical considerations and numerical implementation. *Journal of Engineering Mechanics*, 140(9), 2014, 04014062.
- [17] Capdevielle, S., Grange, S., Dufour, F., Desprez, C., A multifiber beam model coupling torsional warping and damage for reinforced concrete structures. *European Journal of Environmental and Civil Engineering*, 20(8), 2016, 914-935.
- [18] Genoese, A., Genoese, A., Bilotta, A., Garcea, G., A geometrically exact beam model with non-uniform warping coherently derived from the Saint Venant rod. *Engineering Structures*, 68, 2014, 33-46.
- [19] Le Corvec, V., Nonlinear 3d frame element with multi-axial coupling under consideration of local effects. Ph.D. Thesis, University of California, Berkeley, USA, 2012.
- [20] Di Re, P., Addessi, D., Filippou, F.C., 3d beam-column finite element under non-uniform shear stress distribution due to shear and torsion. *ECCOMAS Congress 2016, VII European Congress on Computational Methods in Applied Sciences and Engineering*, 2016.
- [21] Di Re, P., Addessi, D., Filippou, F.C., Mixed 3D beam element with damage plasticity for the analysis of RC members under warping torsion. *Journal of Structural Engineering - ASCE*, 144(6), 2018, 04018064.
- [22] Di Re, P., Addessi, D., A mixed 3D corotational beam with cross-section warping for the analysis of damaging structures under large




displacements. *Meccanica*, 53(6), 2018, 1313-1332.

- [23] Di Re, P., Addessi, D., Paolone, A., Mixed beam formulation with cross-section warping for dynamic analysis of thin-walled structures. *Thin-Walled Structures*, 141, 2019, 554-575.
- [24] Gruttmann, F., Sauer, R., Wagner, W., Shear stresses in prismatic beams with arbitrary cross-sections. *International Journal for Numerical Methods in Engineering*, 45(7), 1999, 865-889.
- [25] Lee, S.W., Kim, Y.H., A new approach to the finite element modelling of beams with warping effect. *International Journal for Numerical Methods in Engineering*, 24(12), 1987, 2327-2341.
- [26] Yoon, K., Lee, P.S., Kim, D.N., An efficient warping model for elastoplastic torsional analysis of composite beams. *Composite Structures*, 178, 2017, 37-49.
- [27] Khoder, N., Grange, S., Sieffert, Y., Enhancement of a two-dimensional multifibre beam element in the case of reinforced concrete structures for taking into account the lateral confinement of concrete due to stirrups. *European Journal of Environmental and Civil Engineering*, 23(5), 2019, 564-585.
- [28] Lee, C.L., Filippou, F.C., Frame elements with mixed formulation for singular section response. *International Journal for Numerical Methods in Engineering*, 78(11), 2009, 1320-1344.
- [29] Neuenhofer, A., Filippou, F.C., Evaluation of nonlinear frame finite-element models. *Journal of Structural Engineering - ASCE*, 123(7), 1997, 958-966.
- [30] Saritas, A., Soydas, O., Variational base and solution strategies for non-linear force-based beam finite elements. *International Journal of Non-linear Mechanics*, 47(3), 2012, 54-64.
- [31] Simo, J.C., Hughes, T.J.R., *Computational inelasticity*. Springer Science & Business Media, 2006.
- [32] Klinkel, S., Govindjee, S., Using finite strain 3D-material models in beam and shell elements. *Engineering Computations*, 2002.
- [33] Zienkiewicz, O.C., Taylor, R.L., *The finite element method for solid and structural mechanics*. Elsevier, 2005.
- [34] Soydas, O., Saritas, A., An accurate nonlinear 3d Timoshenko beam element based on Hu-Washizu functional. *International Journal of Mechanical Sciences*, 74, 2013, 1-14.
- [35] Spacone, E., Filippou, F.C., Taucer, F.F., Fibre beam-column model for non-linear analysis of R/C frames: Part I. Formulation. *Earthquake Engineering & Structural Dynamics*, 25(7), 1996, 711-725.
- [36] Kostic, S.M., Filippou, F.C., Section discretization of fiber beam-column elements for cyclic inelastic response. *Journal of Structural Engineering - ASCE*, 138(5), 2012, 592-601.
- [37] Vlasov, V.Z., *Thin-Walled Elastic Beams*, National Technical Information Service, 1984.
- [38] El Fatmi, R., Non-uniform warping including the effects of torsion and shear forces. Part I: A general beam theory, *International Journal of Solids and Structures*, 44(18-19), 2007, 5912-5929.
- [39] Menegotto, M., Method of analysis for cyclically loaded RC plane frames including changes in geometry and non-elastic behavior of elements under combined normal force and bending. IABSE symposium on resistance and ultimate deformability of structures acted on by well defined repeated loads, 1973, 15-22.
- [40] Addessi, D., Marfia, S. Sacco, E., A plastic nonlocal damage model. *Computer Methods in Applied Mechanics and Engineering*, 191(13-14), 2002, 1291-1310.
- [41] Drucker, D.C., Prager, W., Soil mechanics and plastic analysis or limit design. *Quarterly of Applied Mathematics*, 10(2), 1952, 157-65
- [42] Gatta, C., Addessi, D., Vestroni, F., Static and dynamic nonlinear response of masonry walls. *International Journal of Solids and Structures*, 155, 2018, 291-303.
- [43] Rezaiee-Pajand, M., Sharifian, M., Sharifian, M., Accurate and approximate integrations of Drucker-Prager plasticity with linear isotropic and kinematic hardening. *European Journal of Mechanics-A/Solids*, 30(3), 2011, 345-361.
- [44] Öztekin, E., Pul, S., Hüseim, M., Experimental determination of Drucker-Prager yield criterion parameters for normal and high strength concretes under triaxial compression. *Construction and Building Materials*, 112, 2016, 725-732.
- [45] Strang, G., *Linear algebra and its application*. Thomson, Brooks Cole, 2006.
- [46] Neuenhofer, A., Filippou, F.C., Evaluation of nonlinear frame finite-element models. *Journal of structural engineering*, 123(7), 1997, 958-966.
- [47] Addessi, D., Ciampi, V., A regularized force-based beam element with a damage-plastic section constitutive law. *International Journal for Numerical Methods in Engineering*, 70(5), 2007, 610-629.
- [48] Mazars, J., Kotronis, P., Ragueneau, F., Casaux, G., Using multifiber beams to account for shear and torsion: Applications to concrete structural elements. *Computer Methods in Applied Mechanics and Engineering*, 195(52), 2006, 7264-7281.
- [49] Pegon, P., Plumier, C., Pinto, A., Molina, J., Gonzalez, P., Tognoli, P., U-shaped walls: quasi-static bi-axial test in the X and Y directions - Test report. Technical report, TMR-ICONSTOPICS, Test report, JRC, Ispra, Italy, 2000
- [50] Beyer, K., Dazio, A., Priestley, M.J.N., Quasi-static cyclic tests of two U-shaped reinforced concrete walls. *Journal of Earthquake Engineering*, 12(7), 2008, 1023-1053.
- [51] Bathe, K.J., Dvorkin, E.N., A four-node plate bending element based on Mindlin/Reissner plate theory and a mixed interpolation. *International Journal for Numerical Methods in Engineering*, 21(2), 1985, 367-383.
- [52] Chalioris, C.E., Torsional strengthening of rectangular and flanged beams using carbon fibre-reinforced-polymers-Experimental study. *Construction and Building Materials*, 22(1), 2008, 21-29.
- [53] Basaglia, C., Camotim, D., Silvestre, N., Torsion warping transmission at thin-walled frame joints: Kinematics, modelling and structural response. *Journal of Constructional Steel Research*, 69(1), 2012, 39-53.
- [54] Genoese, A., Genoese, A., Bilotta, A., Garcea, G., A mixed beam model with non-uniform warpings derived from the Saint Venant rod. *Computers & Structures*, 121, 2013, 87-98.
- [55] Addessi, D., Di Re, P., Cimarello, G., Enriched beam finite element models with torsion and shear warping for the analysis of thin-walled structures. *Thin-Walled Structures*, 159, 2021, 107259.
- [56] Taylor, R.L., FEAP-finite element analysis program, 2014. URL: <http://www.ce.berkeley/feap>.

## ORCID iD

Paolo Di Re  <https://orcid.org/0000-0002-3093-2728>

Daniela Addessi  <https://orcid.org/0000-0003-0580-3200>



© 2022 Shahid Chamran University of Ahvaz, Ahvaz, Iran. This article is an open access article distributed under the terms and conditions of the Creative Commons Attribution-NonCommercial 4.0 International (CC BY-NC 4.0 license) (<http://creativecommons.org/licenses/by-nc/4.0/>).

**How to cite this article:** Di Re P., Addessi D. Computational Enhancement of a Mixed 3D Beam Finite Element with Warping and Damage, *J. Appl. Comput. Mech.*, 8(1), 2022, 260–281. <https://doi.org/10.22055/JACM.2021.37948.3120>

**Publisher's Note** Shahid Chamran University of Ahvaz remains neutral with regard to jurisdictional claims in published maps and institutional affiliations.

